

RSC Sustainability

Accepted Manuscript

This article can be cited before page numbers have been issued, to do this please use: X. Huang, M. Gao, S. Wang, L. A. N. Azizah, Y. Yang and D. A. Tafere, *RSC Sustainability*, 2025, DOI: 10.1039/D5SU00555H.



This is an Accepted Manuscript, which has been through the Royal Society of Chemistry peer review process and has been accepted for publication.

Accepted Manuscripts are published online shortly after acceptance, before technical editing, formatting and proof reading. Using this free service, authors can make their results available to the community, in citable form, before we publish the edited article. We will replace this Accepted Manuscript with the edited and formatted Advance Article as soon as it is available.

You can find more information about Accepted Manuscripts in the [Information for Authors](#).

Please note that technical editing may introduce minor changes to the text and/or graphics, which may alter content. The journal's standard [Terms & Conditions](#) and the [Ethical guidelines](#) still apply. In no event shall the Royal Society of Chemistry be held responsible for any errors or omissions in this Accepted Manuscript or any consequences arising from the use of any information it contains.

Sustainability Spotlight Statement

Nitrogen doping modifies the electronic structure, band gap, and surface chemistry of materials, improving performance sustainably. By controlling temperature and doping levels, surface area and multifunctional properties are optimized, enhancing applications in eco-friendly energy storage, catalysis, and gas adsorption. This process reduces waste generation, aligning with green chemistry principles for a more sustainable future.

This review discusses green synthesis methods for various N-doping configurations (pyridinic, graphitic, oxidized N) to promote material sustainability. It highlights eco-friendly activation and carbonization processes that improve structural integrity and electrochemical performance, all while minimizing the environmental footprint.

This section uses density functional theory (DFT) to predict and validate the properties of N-doped materials derived from waste, supporting sustainable practices. It assesses challenges, potential improvements, and future opportunities for applying these green materials in energy storage, gas adsorption, catalysis, and water treatment, contributing to a circular economy and promoting environmental sustainability



Review

Waste-Derived Green N-Doped Materials: Mechanistic Insights, Synthesis, and Comprehensive EvaluationXiang-Mao Huang^a, Mengyao Gao*, Dessie Ashagrie Tafere^a, Shao-Yu Wang^a, Luthfiyyah Annisa Nur Azizah^a, Yan-Ling Yang^aReceived 00th January 20xx,
Accepted 00th January 20xx

DOI: 10.1039/x0xx00000x

Nitrogen (N)-doped materials derived from biomass hold great promise for energy storage, gas adsorption, catalysis, and water treatment, offering an effective strategy for waste valorization. Precise control over temperature and nitrogen doping levels has been shown to enhance surface area and multifunctional properties. This review begins by covering fundamental principles such as band gap and electronegativity, followed by an analysis of N-doping preparation methods, focusing on pyridinic N, graphitic N, and oxidized N and the applications, especially in energy storage, carbon dioxide (CO₂) capture, and catalyst for hydrogen generation. Additionally, density functional theory (DFT) calculations are explored to elucidate the structural and electrochemical properties of N-doped materials. This review seeks to advance the sustainable development of waste-derived green materials by conducting a comprehensive comparative analysis of material activation and carbonization mechanisms. Furthermore, it addresses the challenges, perspectives, and prospects of waste valorisation for green N-doped materials, exploring their potential across diverse applications.

1. Introduction

Our planet is undergoing a rapid energy crisis, accompanied by floods, wildfires, and extreme heat waves. A green reset must be prioritized to place sustainable development at the forefront. This shift is crucial for scientists to effectively address the urgent energy and environmental challenges we now face¹. In response to the high demand for renewable resources, various types of biomass waste have gained significant attention as precursors for nitrogen-doped (N-doped) materials². These include animal-derived wastes such as fish bone³, shrimp shell^{4,5}, chicken feather⁶, animal manure⁷⁻⁹ and animal collagen¹⁰, plant-based waste, including orange peel¹¹, tamarind shell¹², algae¹³, sugar cane bagasse¹⁴, soybean¹⁵ and sunflower seeds¹⁶. These biomass resources offer a promising route for the synthesis of N-doped carbon materials, due to their low cost, wide availability, and rich composition of heteroatoms such as O, N, and S, as well as trace metals¹⁵⁻¹⁸.

Green chemistry is associated design of chemical products and processes that minimize the use and generation of hazardous substances¹⁹⁻²³. In this context, it is important to highlight the role of activated carbon derived from lignocellulosic biomass, which includes carbon materials obtained from grasses, wood, corn stalks, and other crop residues. These carbon materials exhibit excellent electrical conductivity, a well-developed porous structure, and high

specific surface area, thereby facilitating efficient charge transport and providing ample space for ion storage²⁴.

Due to the unique combination of renewability, low cost, natural abundance, sustainability, and microstructural tunability, biomass-derived carbon materials have been widely applied in various fields¹⁶⁻¹⁸, including air pollution control²⁵, water desalination, wastewater treatment²⁶, supercapacitor²⁷, greenhouse gas emissions²⁸, membrane technology, electrochemistry¹⁸, and energy storage^{26,29}. Resources such as the biomass (lignocellulose)³⁰⁻³³, wood biomass³⁴ and agricultural residue/by products have been considered as main materials for the N-Doping applications³⁵⁻³⁹. In particular, waste-derived biomass such as coconut shells²⁵, cotton-based⁴⁰, sugarcane⁴¹, macroalgae¹³, water hyacinth and water lettuce³³, has shown great potential as precursors for activated carbon, suitable not only for energy storage but also for various environmental and catalytic applications.

Biomass has emerged as a sustainable source for green carbon materials through processes involving nitrogen incorporation, pre-carbonization, and activation, which enhance surface area and introduce key functional groups⁴². Figure 1 schematically represents these steps, emphasizing the structural evolution of biomass into functionalized carbon. Nitrogen atoms play a pivotal role in modifying the structure^{16,43-46}, morphology^{16,43-46} and electrochemical properties⁴⁷⁻⁴⁹ of carbon materials. Activated carbon could be considered as a candidate for the excellent high storage performance of N atoms, where those materials are doping in the structure of materials and present on the surface of materials. They can form functional groups, such as amine (-NH₂) and nitroso (-NO). Furthermore, nitrogen atoms can be incorporated directly into

^a Department of Chemical Engineering, National Taiwan University of Science and Technology, Taipei 10607, Taiwan. E-mail: mygao@mail.ntust.edu.tw



the carbon lattice in several forms pyridinic-N, pyrrolic-N, graphitic-N, oxidized-N, and graphite-N²⁷ each contributing distinct electronic and catalytic properties. Nitrogen-doped carbon derived from biomass demonstrates remarkable potential in a range of applications. In this review, we focus particularly on its utility in energy storage systems, carbon dioxide (CO₂) capture, and as a catalyst for hydrogen evolution reactions.

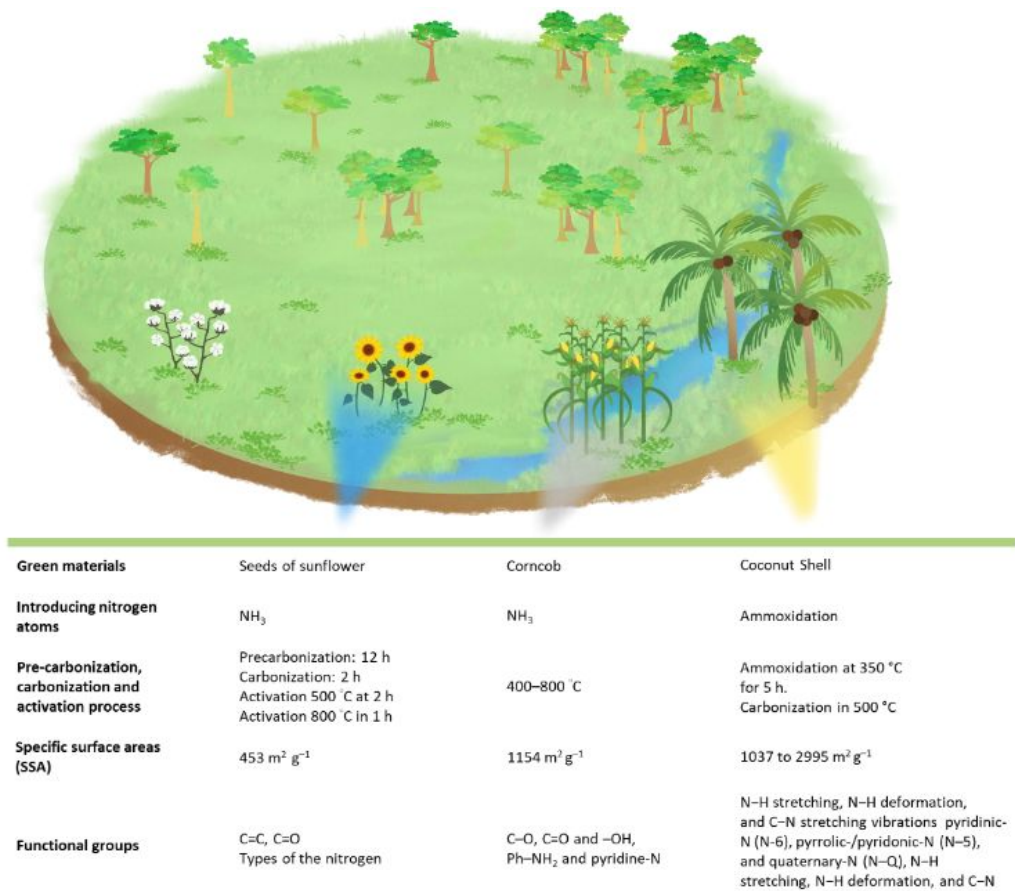


Fig. 1. Illustration depicting plants as a precursor for green materials, showcasing the introduction of nitrogen atoms, pre-carbonization and activation processes, enhancement of specific surface area, and incorporation of functional groups for improved functionality.

To obtain N-doped materials, various processes have been developed, including pre-carbonization, carbonization, and activation (either physical or chemical). Pre-carbonization is the initial phase of carbonization, during which organic or polymeric precursors undergo partial thermal decomposition. In this stage, the material is subjected to moderate temperatures ranging from 200 to 400 °C. Carbonization is the process of converting organic materials into carbon or carbon-rich residues through pyrolysis. Activation, whether physical or chemical, enhances the surface area and porosity of the carbonized materials. This step often facilitates the preparation

of the material for subsequent high-temperature carbonization by stabilizing its structure.²⁵ The type and distribution of nitrogen functionalities, previously discussed, are strongly influenced by these processing conditions. Specifically, carbonization temperature, nitrogen precursors, and activation method govern the incorporation of nitrogen into the carbon matrix, impacting both the structural and electronic characteristics of the final material. A summary of common activation agents and their respective advantages and limitations is presented in Table 1.

Table 1. Advantages and disadvantages of different precursors in the activation of materials

View Article Online

DOI: 10.1039/D5SU00555H

Activator	Advantages	Disadvantages	References
NH ₃	Higher material density, cost-efficient, environmentally friendly, high material density.	Lower surface area.	50
CO ₂	Activation occurs at the solid–gas interface, CO ₂ generates large micro and mesopores, Increasing catalytic activity.	Leading to incomplete N-doping.	51
KOH	High performance, high specific surface area, hierarchical porous structures, effective migration channels for the electrolytic ions, leading to high rate performances, generate high nanopores.	Low material density, corrosion behavior, not environmentally friendly, KOH requires relatively high temperature (> 600°C), corrosive.	15, 52–55
K ₂ FeO ₄	Powerful oxidizing agent via different pH, environmentally friendly oxidant, improve magnetization and pore size, lower temperatures.	Unstable and restrict scale application and development in industrial the large applications.	56–60
ZnCl ₂	Improve the carbon content, lower yield, preventing hyperactivation, better control on porosity, and more micropores.	Problem with dosage, expensive, improper tuned pore structure and surface properties.	61–63
H ₃ PO ₄	Cost-less, less corrosive, suitable crosslinking and dehydrating agent, low toxicity.	Depending on impregnation solution because of high polar character.	64–66
Na ₂ CO ₃	Depending on the temperature, optimal performance, and high surface area.	Microporous solids and relatively small external area.	67, 68

This review provides an in-depth overview of the synthesis methods for various waste-derived N-doped materials, with an emphasis on environmentally friendly and sustainable production strategies.^{25, 50, 61} We explore green activation approaches, structural evolution during thermal processing, and the resulting physicochemical properties of N-doped carbon. The mechanisms governing nitrogen doping efficiency and the impact of process variables are critically examined. Additionally, we discuss post-synthesis modifications, and evaluate the performance of these materials in applications such as adsorption, catalysis, membrane separation, and electrochemical energy storage. Finally, the review concludes with a forward-looking perspective on future challenges and opportunities for the large-scale implementation of green, waste-derived N-doped materials in circular technologies.

2. Principles for enhancing sustainable approach to waste valorization

2.1. Band gap

The relationship between band gap engineering and nitrogen-doped carbon materials is central to their performance in energy conversion and storage applications. The band gap is defined as the energy difference between the valence band and conduction band, which determines a material's ability to conduct electricity⁶⁹. Nitrogen doping introduces new electronic states within the carbon lattice, effectively narrowing the band gap and enabling easier electron transitions. This facilitates enhanced charge transport, improving the material's

conductivity and reactivity. The type (e.g., pyridinic, graphitic, oxidized) and concentration of nitrogen dopants strongly influence the extent of band gap reduction and the formation of localized states. These modifications directly affect the material's optical and electronic behavior, making N-doped carbon highly suitable for photocatalysis, electrocatalysis, and electrochemical energy storage (e.g., batteries and supercapacitors). Figure 2a demonstrates this concept by comparing materials with no band gap, a small band gap, and a large band gap, illustrating how smaller gaps correlate with higher conductivity due to facilitated electron transition.

2.2. Electronegativity

Electronegativity, the tendency of an atom to attract electrons in a chemical bond, plays a key role in the charge redistribution in N-doped carbon materials⁷⁰. Nitrogen, with a higher electronegativity (3.04) than carbon (2.55), draws electron density towards itself when doped into a carbon matrix, resulting in localized dipoles and a shift in electron density away from adjacent carbon atoms. This polarization effect, visualized in Figure 2b, leads to charge accumulation around nitrogen (δ^-) and depletion near carbon atoms (δ^+). Such asymmetry modifies the electronic structure, contributes to band gap narrowing, and enhances electrical conductivity⁷¹. This redistribution of charge not only improves electron mobility but also activates new reactive sites, especially relevant in oxygen reduction reactions (ORR) and other catalytic pathways. In energy storage systems, this altered charge landscape promotes efficient ion adsorption and fast electron transfer,



enhancing both capacity and rate performance. From a theoretical perspective, electronegativity is not directly measurable as an energy value, but is inferred based on ionization energy, electron affinity, and atomic size. It generally increases across a period and decreases down a group. For instance, nonmetals such as O₂ and N₂, with high electronegativity, tend to attract shared electrons more strongly in covalent bonds. When electrons are shared

unequally, as is the case in N-doped carbons, the stronger pull of nitrogen results in electron density distortion that affects geometry and reactivity. This charge imbalance leads to structural relaxation and formation of localized electronic states, further validating the role of electronegativity in improving catalytic efficiency and electronic conductivity in green N-doped materials.

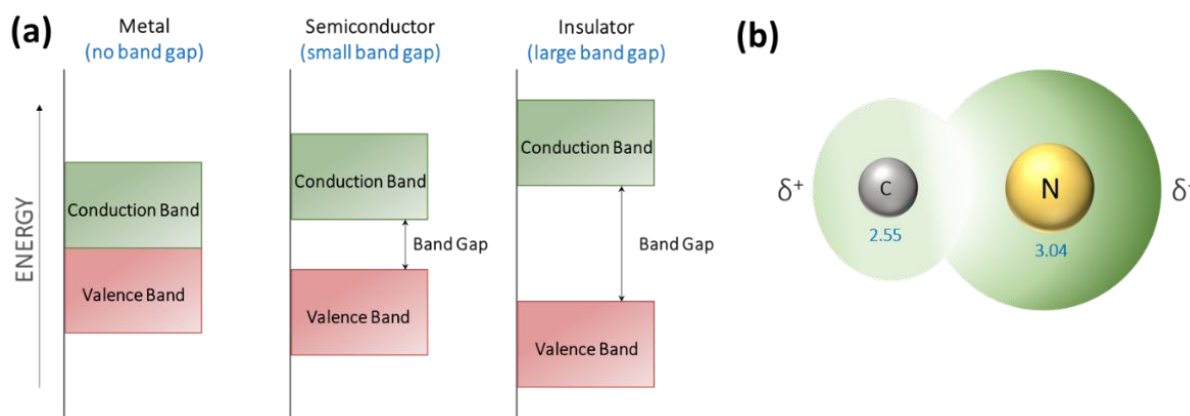


Fig. 2. Schematic representation of (a) the effect of band gap size on electronic conductivity, showing materials with no band gap, small band gap, and large band gap. Smaller band gaps enable easier electron transition and higher conductivity. (b) Electronegativity difference between nitrogen (N) and carbon (C), illustrating charge redistribution due to N-doping. Nitrogen's higher electronegativity leads to electron accumulation (δ^-) around N and depletion (δ^+) around adjacent carbon atoms, enhancing the material's reactivity and electronic properties.

2.3. Electrical conductivity

Electrical conductivity is a critical parameter in evaluating the electronic behavior of materials, especially semiconductors and carbon-based nanostructures such as single-walled carbon nanotubes (SWCNTs)⁷². The conductivity of semiconductor materials depends on the concentration of charge carriers. At elevated temperatures (e.g., 410-450 K), semiconductors exhibit intrinsic conductivity, wherein electrons at the top of the valence band are thermally excited to the conduction band, leaving behind holes⁷³. Each excited electron creates a corresponding hole, resulting in equal concentrations of electrons and holes. The carrier concentration (N_i) in such intrinsic semiconductors can be expressed using classical Boltzmann statistics⁷⁴.

$$N_i = N = P = ZT^{\frac{3}{2}} \exp\left(-\frac{E_g}{2kT}\right) \quad (1)$$

where Z is a constant, T is the thermodynamic temperature, k is the Boltzmann constant, and E_g is the band gap width of the semiconductor. The carrier concentration (N_i) of the semiconductor material at elevated temperatures demonstrates a direct proportionality to the cube root of temperature.

The intrinsic conductivity of the high-temperature conducting region can be formulated as follows:

$$\sigma = Z \exp\left(-\frac{E_g}{2kT}\right) \quad (2)$$

After applying the logarithmic transformation to eq 2, the slope of the resulting line can be determined via fitting curve analysis, allowing for the expression of the band gap width:

$$E_g = -2k \Delta T \ln \sigma \quad (3)$$

The electrical conductivity was determined by obtaining the I-V curve at different doping concentrations and different temperatures. The conductivity formula is described as follows.

$$\sigma = \frac{I \times L}{V \times A} \quad (4)$$

where I is the electric current, V is the applied voltage, L is the average length of the SWCNTs, and A is the average cross-sectional area obtained from transmission electron microscopy (TEM) characterization. The enhanced conductivity in N-doped carbon materials is primarily attributed to charge redistribution driven by electronegativity differences, which alters the band structure and improves charge mobility. As a result, these materials demonstrate excellent potential in applications such as electrocatalysis, batteries, supercapacitors, and photocatalysis, where efficient electron transfer is essential.



3. Different N-doping types based on carbonization temperatures

Carbonization temperature plays a critical role in determining the porosity, elemental composition, and nitrogen configuration of biomass-derived N-doped carbon materials. These materials typically exhibit a hierarchical porous structure, consisting of micropores (<2 nm), mesopores (2-50 nm), and macropores (>50 nm)⁷⁵, which is essential for optimizing ion diffusion, mass transport, and surface reactivity in electrochemical systems.

As the carbonization temperature increases from 600 °C to 950 °C, a significant transformation in chemical composition is observed. Specifically, the nitrogen content decreases from 6.54% to 0.92%, while carbon content increases from 74.80% to 88.19% and oxygen content decreases from 18.94% to 10.08%. This shift reflects enhanced thermal decomposition, deoxygenation, and graphitic ordering within the carbon matrix. The C/O molar ratio, which reflects the material's reduction capacity and degree of graphitization, correspondingly increases with temperature, peaking at 11.67 at 950 °C (Table 2).

Table 2. Elemental Composition and C/O Molar Ratios of N-Doped Carbon at Various Carbonization Temperatures

Carbonization temperature / °C	N (%)	C (%)	S (%)	O (%)	C/O molar ratio
600	6.54	74.80	0.22	18.94	5.26
650	4.25	76.38	0.20	16.25	6.26
700	3.31	76.73	0.19	18.88	5.42
750	2.32	80.81	0.16	16.15	6.67
800	2.48	78.09	0.45	17.47	5.96
850	1.14	84.96	0.16	13.38	8.47
900	1.05	84.61	0.21	13.31	8.49
950	0.92	88.19	0.23	10.08	11.67

The evolution of nitrogen bonding environments with temperature was investigated using X-ray photoelectron spectroscopy (XPS). At 600 °C, the N 1s spectrum exhibits peaks corresponding to pyrrolic-N (~400.0 eV) and pyridinic-N (~400.4 eV). As temperature increases, pyridinic-N decreases significantly, and quaternary-N (graphitic-N) emerges,

indicating ring-opening reactions and nitrogen rearrangement. Between 750 °C and 950 °C, both quaternary-N and pyrrolic-N contents gradually decline due to thermal decomposition. The order of thermal stability is: quaternary-N > pyrrolic-N > pyridinic-N, highlighting the prevalence of graphitic nitrogen at higher temperatures.



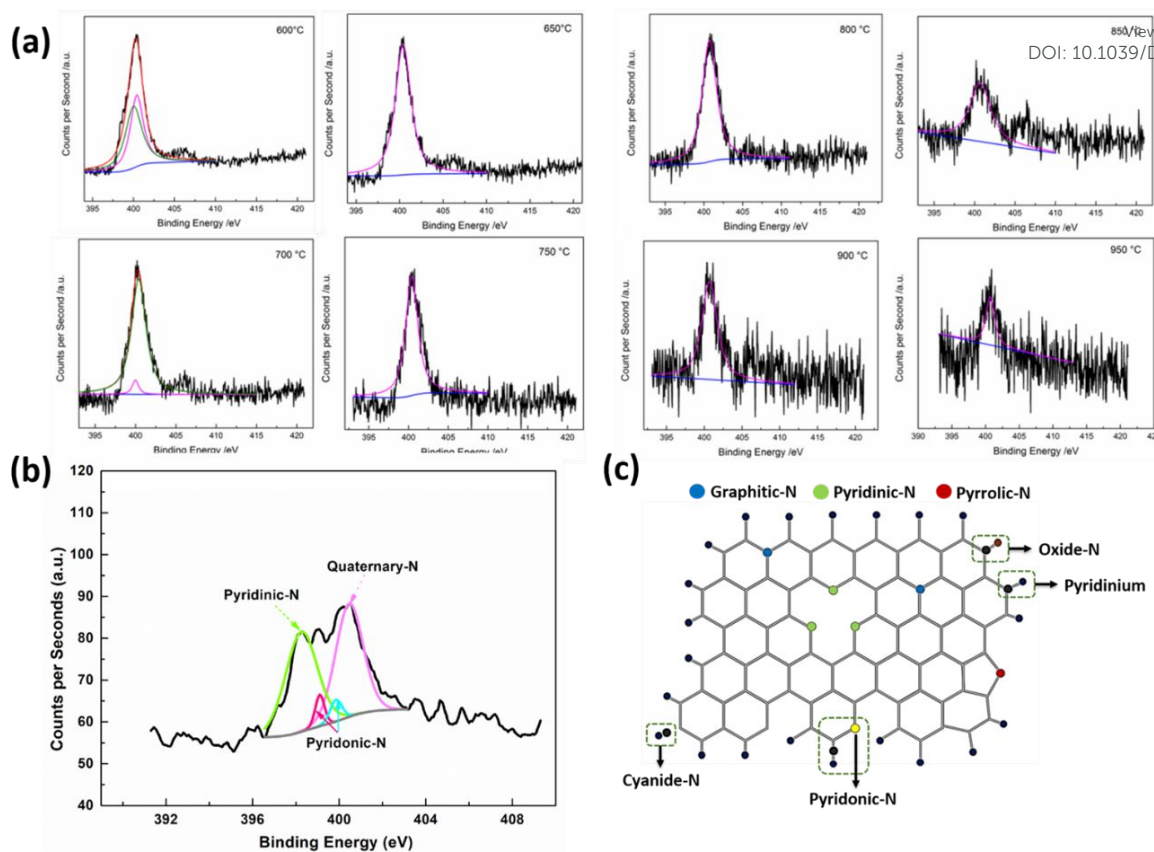


Fig. 3 (a) High-resolution N 1s XPS spectra of carbonized materials at various temperatures, showing the transformation of pyridinic and pyrrolic N into quaternary N. (b) Bonding configurations and relative thermal stabilities of pyridinic-N, pyrrolic-N, and graphitic-N. (c) Schematic illustration of nitrogen species transformation pathways during thermal treatment. Adapted from Ref. ⁷⁶.

Figure 3a clearly shows this spectral evolution: pyridinic- and pyrrolic-N dominate at lower temperatures, while quaternary-N intensifies at elevated temperatures. Figure 3b outlines the bonding configurations of each nitrogen type: pyridinic-N at graphene edges, pyrrolic-N within five-membered rings, and quaternary-N replacing a carbon atom in the graphitic plane. Figure 3c summarizes the thermally induced transitions, emphasizing how increasing temperature promotes the conversion of labile nitrogen species into more stable graphitic configurations.

These nitrogen types directly influence electrochemical behaviour. Pyridinic-N, bonded to two carbon atoms, donates one p-electron to the π -system, facilitating charge delocalization and catalysis (e.g., ORR). Pyrrolic-N, part of a five-membered ring, donates two p-electrons and contributes to redox processes. Quaternary-N, embedded within the graphitic framework, improves conductivity and structural integrity, essential for applications in oxygen reduction, oxygen evolution, and supercapacitor systems ^{77,78}. Notably, pyrrolic-N is gradually converted into graphitic-N at temperatures above 800 °C, further enhancing the electrical performance and stability of the material.

Complementary XPS analysis of C 1s and O 1s spectra confirms the presence of functional groups such as C-C, C-O, C-N, O=C, O-C, and O-N, which evolve with temperature and influence

surface reactivity ^{14, 15, 17}. These bonding states are quantitatively determined using the electron binding energy equation:

$$E_{\text{binding}} = E_{\text{photon}} - (E_{\text{kinetic}} + \phi) \quad (5)$$

where E_{binding} is the binding energy (BE) of the electron measured relative to the chemical potential, E_{photon} is the energy of the X-ray photons being used, E_{kinetic} is the kinetic energy of the electron as measured by the instrument and ϕ is a work function-like term for the specific surface of the material, which in real measurements includes a small correction by the instrument's work function because of the contact potential.

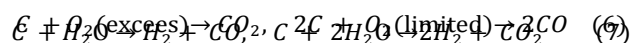
4. Effect of activation on hierarchical porous structure

In the preparation of porous carbon materials using activation methods, the raw materials are typically subjected to a pre-carbonization treatment known as the carbonization process. The main objective is to eliminate volatile components from the organic matter and increase carbon content, forming an initial pore structure suitable for subsequent activation. The carbonization temperature is generally determined based on



thermogravimetric analysis (TGA). Parameters such as heating rate, gas flow rate, and carbonization time influence the physicochemical properties of the resulting carbon. Excessively high carbonization temperatures produce dense structures with low porosity, hindering activation, while low temperatures yield porous but mechanically weak precursors⁷⁹. Thus, optimized carbonization conditions tailored to the feedstock are essential.

Physical activation involves heating the carbonized material at high temperatures using oxidizing gases such as steam, CO₂, O₂, and air to develop a porous structure within the pyrolysis product⁸⁰. During activation, the primary process involves selective chemical reactions between the activation gas and the carbon atoms on the material's surface, forming volatile gases that etch the material and create pores. The specific reactions are described as follows:

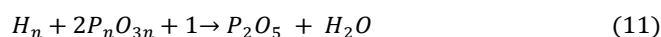
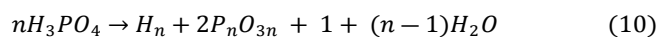
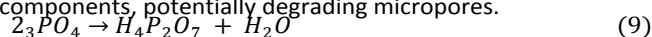


The temperature for physical activation is generally controlled within the range of 800-1000 °C. If the activation temperature is too low, the prepared porous carbon material will have a low specific surface area and underdeveloped pore structure. Conversely, if the activation temperature is too high, it will result in excessive carbon loss, affecting the yield. While this method introduces no impurities and avoids environmental contamination, it is energy-intensive.

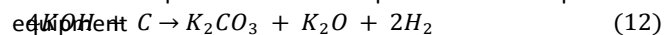
Chemical activation involves impregnating the precursor raw material with chemical activators, followed by carbonization and activation in an inert gas medium. Common activators include alkaline activators (KOH, NaOH), acidic activators (H₃PO₄, H₂SO₄), and salts (ZnCl₂, K₂CO₃, Na₂CO₃)⁸¹. In China, the most common method for producing activated carbon is using ZnCl₂ activation. During activation, ZnCl₂ has a strong dehydrating effect, causing the H and O elements in the raw material to be removed as H₂O(g), forming a developed porous structure. In contrast, using H₃PO₄ as an activator has the advantage of a lower activation temperature, typically between 300-350 °C, resulting in porous carbon materials with rich mesoporous structures. This method is also cost-effective, less toxic, and widely adopted in the United States. Currently, KOH is the most commonly used activator for preparing high-performance porous carbon materials. Using KOH as an activator often results in porous carbon materials with a high specific surface area and well-developed microporous structure. Additionally, the pore size of the prepared porous carbon materials can be controlled by adjusting the amount of KOH used.

During the carbonization process, ZnCl₂, with a low melting point (238 °C), penetrates the precursor material *in situ*, serving as a template to generate interconnected pores. Simultaneously, the activation effect of ZnCl₂ reduces oxygen content and enhances electrical conductivity. In phosphate activation, at 400 °C, P-species doping induces lattice distortion or expands the (002) plane spacing, while partial oxidation of

carbonaceous organics forms P-O-C structures. Phosphate and polyphosphate species form via interactions between H₃PO₄ and the organic matrix, attaching to cross-linked polymer fragments and exposing phosphate peaks, including PO₂ and HPO₃. With further temperature increases, H₃PO₄ undergoes condensation and dehydration, converting into pyrophosphoric acid (H₄P₂O₇), polyphosphate (H_{n+2}P_nO_{3n+1}), and eventually phosphorus pentoxide (P₂O₅). P₂O₅ strongly oxidizes organic components, potentially degrading micropores.



For the KOH activation mechanism, it is relatively well established. The specific reactions are shown in equations. Compared to physical activation, chemical activation occurs at lower temperatures and produces porous carbon materials with higher specific surface areas and more controllable pore structures. However, the corrosive nature of acidic or alkaline activators imposes stricter requirements on production equipment.



The chemical physical activation method combines chemical activation and physical activation. Typically, the raw materials are first mixed with chemical activators, and then oxidizing gases (i.e., oxygen, steam, or CO₂) are introduced and heated simultaneously. This hybrid method enhances reactivity and pore formation, resulting in porous carbon materials with high specific surface area and abundant mesoporosity. Additionally, this method can introduce functional groups onto the carbon surface, imparting special properties for targeted applications.

N-doping methods significantly increase the number of electroactive sites, improving the catalytic and electronic properties of carbon materials⁸²⁻⁹¹. The addition of N₂⁹² and hydrogen bonding⁹³ enhances surface polarity and electrostatic interactions⁹², thus modifying the structure. This section describes the N-doping process, starting from carbonization followed by activation of waste-based biomass, ultimately yielding nitrogen-doped porous carbon. From this perspective, sustainable valorization of waste materials can be successfully achieved. Generally, biomass-derived porous carbon can be applied in energy storage²⁴, CO₂ capture⁹⁴, and catalysis⁹⁵, as shown in Figure 4.

X-ray photoelectron spectroscopy (XPS) is recommended to evaluate the effects of processing temperature on nitrogen bonding and to locate specific nitrogen configurations such as pyridinic-N, quaternary-N, and graphitic-N. The advantages of chemical activation include high porosity²⁵, large surface area and microporosity²⁷, rapid processing, high carbon yield, energy efficiency [88], shorter soaking times, and lower operating temperatures^{96, 97}. In general, chemical activation facilitates hydrolysis⁹⁷. On the other hand, it is associated with environmental impact²⁵, higher temperature requirements, extended reaction time, and increased equipment demands⁹⁸.



Review

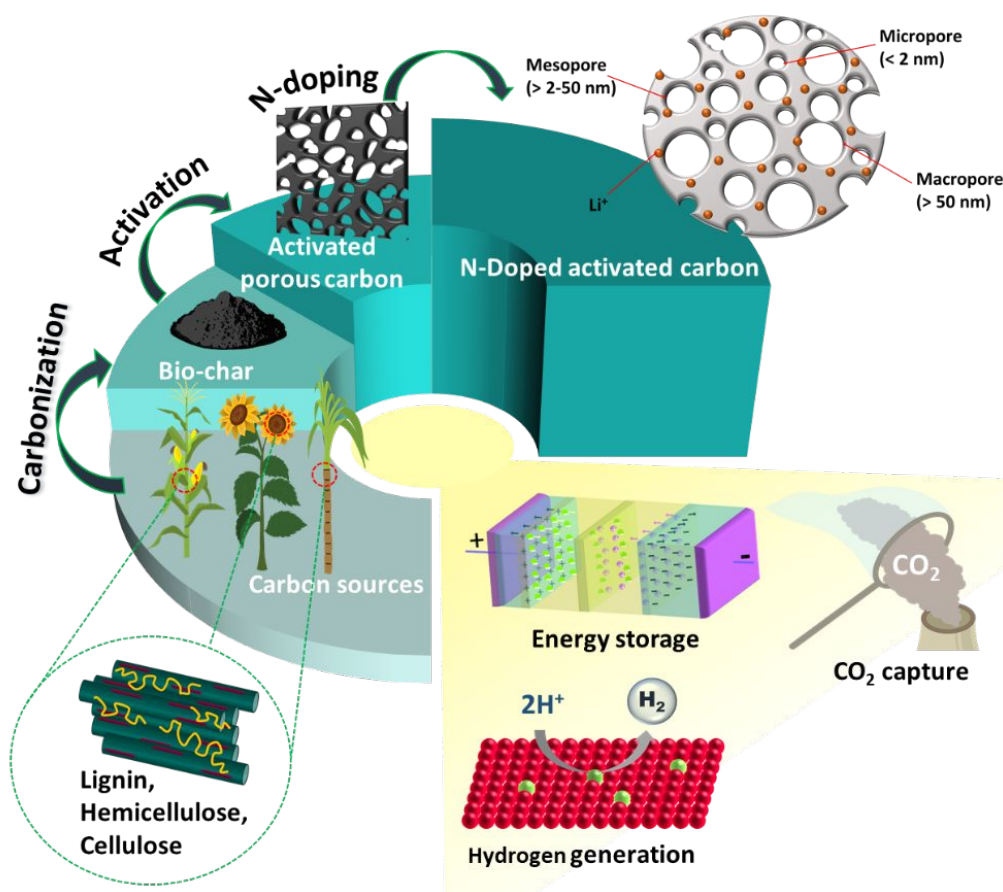


Fig. 4. Waste-derived carbon materials with porous structures and nitrogen doping, formed through carbonization and activation. These features enhance the interaction between water and the material surface, enabling applications in energy storage, CO_2 capture, and hydrogen evolution.

5. Methods of nitrogen-doping porous carbon: activation, carbonation, and post-treatment

The incorporation of nitrogen into porous carbon frameworks significantly modifies the surface chemistry, enhances porosity, and improves electrochemical properties, making it a pivotal strategy for advancing biomass-derived carbon materials^{42, 94}. Functional groups such as carbonyl (C=O), hydroxyl (-OH), and carboxyl (-COOH) serve as key indicators of successful surface modification⁹⁹. The dissociation of C-O and C-N bonds is facilitated by p- π conjugation and the presence of low-basicity heterocyclic nitrogen species (e.g., pyrrole, pyridine). When embedded in a hydrogen-rich matrix, nitrogen-containing sites promote the binding of hydrogen radicals, boost redox activity, and redistribute electron density across the carbon skeleton. Thus, N-doping becomes a strategic tool to tailor electronic

properties and enhance functionality in applications like energy storage, catalysis, and adsorption.

5.1. Nitrogen doping through carbonization of biomass-derived materials.

Numerous studies have conducted N-doping syntheses, namely NH_3 , ammoxidation, and urea, then use the chemical activation with potassium hydroxide (KOH) in order to obtain activated carbon from biomass for various applications and it indicates unique structures^{12, 14, 16, 17, 40, 100}. KOH gives effective process, effective migration channel, sufficient adsorption, better capacitance^{55, 101}, high specific surface area⁵⁴, porous texture¹⁰² and high development of porous structures^{55, 101}.

Table 3 presents the comparison of NH_3 , ammoxidation and urea with KOH chemical activation. For instance,⁴⁰ used NH_3 for synthesizing the cotton to generate cotton-based carbon fibers (CCFs) with turbo static carbon, then activated with KOH.



Carbonization was conducted in a conventional tube furnace, where the temperatures were controlled at 700, 800, and 900 °C for 2 h, heating rate and flow rate of N₂ gas were set up at 5 °C min⁻¹ and 100 mL min⁻¹, respectively. High specific surface area in different temperatures at 700, 800, and 900 °C were 318.20, 602.10, and 778.60 m² g⁻¹, respectively. From this point of view, the higher temperature generates larger surface area with the value of 778.60 m² g⁻¹, and with high mesopore compositions of the material¹⁰³. According to¹⁰⁴, this material can be considered in the supercapacitor application. It is supported with the finding that electrical conductivity with value 0.04 S cm² can be obtained with temperature at 900 °C. In this concept, higher carbonization temperature increases the conductivity in terms of preparation and carbonization of CCFs in NH₃. Vice versa, higher carbonization temperature decreases the percentage of micropore during carbonizing temperature, and it can be found that carbonization at 800 °C shows a greater result compared to 900 °C with value more than 3 nm, from the

peak evaluation more than 3 nm⁴⁰. Moreover, XPS analysis confirm that composition of O increase from 8.52–10.50% after the CCFs carbonization with N₂. Because of the finding of O1s, it is clear, that O element exists in the material. It is also supported by the finding of C = O, C – O – C, C – O – H, and COOH from materials. In more detail, an existence of C = O functional group plays a major role in the electrochemical capacitance associated with the faradic reaction^{105, 106} because of the redox reaction of N₂-based O₂ groups, where O₂ functional groups play a major role as electron acceptors¹⁰⁷ and N₂ plays an integral role as electron-donors¹⁰⁸. Also, parts of C – OH groups are converted to C = O, confirming the increase of C = O bonds¹⁰⁵. Thus, it can be understood that higher temperature of synthesize material improves the electrochemical capacitance because of the presence of O in C = O in the materials.

Table 3. Nitrogen doping through carbonization of biomass-derived materials.

Nitrogen doping	Green materials	Synthesize methods	Carbonization (°C)	Surface area (m ² g ⁻¹)	Functional groups	Ref.
NH ₃	Cotton	Pre-carbonization: N/A	N/A	318.2~778.6	C=O, C–O–C, C–O–H, COOH	40
		Carbonization: 2 h	700, 800, 900			
		Activation: N/A	N/A			
NH ₃	Licorice root	Pre-carbonization: N/A	60	392.9~1257.8	O=C, C–O/C–OH and C–OOH	17
		Carbonization: 2 h	750			
		Activation: N/A	N/A			
NH ₃	Seeds of sun flower	Pre-carbonization: 12 h	N/A	453.0	C=C, C=O	16
		Carbonization: 2 h	N/A			
		Activation: 2h	500, 800			
NH ₃	Soybean	Pre-carbonization: N/A	N/A	392.9~1257.8	O=C, C–O/C–OH and C–OOH	15
		Carbonization: 2 h	800°C			
		Activation: N/A	N/A			
NH ₃	Corncob	Pre-carbonization: N/A	N/A	1154.0	C–O, C=O and –OH, Ph–NH ₂ and pyridine-N	109
		Carbonization: 2 h	400-800			
		Activation: N/A	N/A			
Ammonia	Coconut shell	Pre-carbonization: 5 h	N/A	1037.0~2995.0	N–H stretching, N–H deformation, and C–N stretching vibrations pyridinic-N (N–6), pyrrolic-pyridinic-N (N–5), and quaternary-N (N–Q), N–H stretching, N–H deformation, and C–N	100
		Carbonization: 2 h	500			
		Activation: N/A	N/A			
Urea	Sugar cane bagasse	Pre-carbonization: N/A	N/A	2905.0	–OH and –COOH, C=C–C–N, C–O and CN and C=O, O1s = O–N, O=C and O–C, N 1s = pyridinic-N (N–6), pyrrolic N (N–5), quaternary N (N–Q), and oxidized nitrogen atoms (N–X).	14
		Carbonization: N/A	N/A			
		Activation: 2 h	800			



Urea	Tamarind shell	Pre-carbonization: 45 min	350	410.0	C–C, C=O and C–C=O bonds	¹²
		Carbonization: 2 h	800			
		Activation: N/A	N/A			
Urea	Enteromorpha clathrate	Pre-carbonization: 45 min	550	97.0~217.3	O–H, C=O, C=H, and C–H, C=N	¹¹⁰
		Carbonization: 2 h	800			
		Activation: N/A	N/A			
Urea	Chlorella sp and Spirulina sp	Pre-carbonization: N/A	95	5.0-602.8	N–H and/or –OH, CH ₂ , N–H, C = O, and C–N	¹³
		Carbonization: 2 h	N/A			
		Activation: 90 min	N/A			
Urea	Orange peel	Pre-carbonization: 24 h	210	589.0~590.0	N/A	¹¹
		Carbonization: 2 h	N/A			
		Activation: 90 min	600–700			

Gao. et al. synthesized the activated carbon from licorice residues root derived from nitrogen doping porous carbon (NP-LRC)¹⁷. One gram of licorice root powder was mixed with NH₄Cl and 1 g of KOH. Thereafter, tube furnace was used for heating the materials, and carbon materials were dried in a vacuum oven at 60 °C for 12 h, and carbonization materials was performed at 750 °C for 2 h. NP-LRC shows the surface area with the value of 1257.80 m² g⁻¹, with the pore size ranging from 2–5 nm, indicating the superior mesoporous structures. Also, larger specific surface area and mesopores increases the permeation of electrolyte penetration and ion adsorption. According to ¹¹¹ the presence of O and N heteroatoms creates redox reaction more efficient. Binding energies are associated with the C (C1s) atoms that connected with O (O1s) atom with the single bond or two O atoms⁵⁵. Thus, the existence of O and N in the sample, confirms the successful synthesis of materials.

A process of amoxidation is performed with the mixing of NH₃ to material to create an activated carbon¹⁰⁰. The coconut shell via the oxygen peroxide then treated with the amoxidation process and KOH for the activation for synthesizing the nitrogen-doping porous carbon. Carbonization was performed via nitrogen flow rate 200 mL min⁻¹, heating at 500 °C with the heating rate of 5 °C/min. Carbonization was conducted with size ranging from 100–140 mesh was used as a precursor. Amoxidation was conducted with the mixture of ammonia (NH₃) and air at the ratio of 1:10. Carbonization was conducted at 500 °C for 2 h. After that, it is cooled in the N₂ atmosphere. Furthermore, amoxidation was performed at 350 °C for 5 h. Results indicated that surface area was obtained at the value ranging from 1037–2995 m²g⁻¹. Also, average pore diameters ranging from 0.6 to 0.7 nm, increasing the size of micropores. Functional groups, namely, N–H and C–N are found after activation. Moreover, N species was known as pyridinic (N-6), pyrrolic/pyridinic (N-5) and quaternary-N (N-Q).

Carbonization of urea is used for biomass, then activated via KOH has been conducted by many scholars to derive activated carbon from sugar cane bagasse¹⁴, tamarind shell¹²,

macroalgae¹³, orange peel¹¹ and Enteromorpha clathrata¹¹⁰. Urea has been known as its non-toxic, inexpensive and environmental friendly¹¹².¹⁴ synthesizes 5 g of sugar cane bagasse with urea (5 g), KOH (5 g) were mixed in 100 mL of deionized water and kept for 2 h. Drying process of the mixing precursor at 60 °C, then heated at 800 °C. the as-prepared sugar cane -based material with specific surface area of 2905.4 m² g⁻¹. In this process, urea interacts with –OH and –COOH from the cellulose and lignin in order to form H₂ bonds. Furthermore, C1s refers to functional groups, namely, C=O, C–C, C–O, and C–N. Then, O1s, which exists in the materials, O–N, O=C, and O–C. Lastly, N1s refers to pyridinic-N (N-6), pyrrolic N (N-5), quaternary N (N-Q) and oxidized N₂ atoms (N-X). Furthermore, ¹¹⁰ assess the activated carbon derived from the Enteromorpha clathrata, synthesizing with urea and activated with KOH in the tubular furnace. Then, temperature was controlled at 550 °C at the heating rate of 5 °C min⁻¹ in 60 min and temperature after activation was controlled at 800 °C. Finally, the activation of materials with KOH after pre-carbonization and carbonization of N-doped biomass leads to varying results in functional groups, surface structures, and pore volumes. The presence of N and O atoms in the material plays a crucial role in bonding with C, influencing the material's properties.

5.2. Comparative Analysis of Chemical Activation Processes Using Different Methods

5.2.1. Sodium carbonate

Ilnicka and Lukaszewicz synthesized nitrogen-rich nanoporous activated carbon from chitosan using Na₂CO₃ activation¹¹³. Carbonization (600–900 °C, N₂) and urea doping (for its high N content and solubility) were applied. Activation at 600 °C with 1.93 M Na₂CO₃ resulted in N₂ content of 2.4–13.1 wt.% and surface areas up to 441 m² g⁻¹ (non-urea) but reduced to 121 m² g⁻¹ with urea. XPS confirmed C–N bonding (sp², sp³), including pyridinic (398 eV), pyrrolic (399.8 eV), quaternary (400.9 eV), and N-oxygen species (403.2 eV). Maximum surface areas were 1101–1148 m² g⁻¹ (700–800 °C) with 3.5% surface N₂.⁶⁷ prepared activated carbon from poplar wood via carbonization at 800–



900 °C under N₂ flow. The highest surface area and pore volume reached ~1580 m²/g and ~0.886 cm³g⁻¹. Functional groups such as C-H, O-H, C-O, C=O, and C=C were present, with -CH-CH₂-CH₃ indicating aliphatic stretching. Notably, C≡C appeared due to Na₂CO₃ activation, which influenced functional group composition. Na₂CO₃ activation enhanced material performance and facilitated pyridinic-type N formation, with temperature playing a key role in N-doping.

5.2.2. Activation using orthophosphoric acid

Carbonization with N-doping and chemical activation using orthophosphoric acid (H₃PO₄) has been widely studied for biomass processing. H₃PO₄ is often chosen for its ability to enhance structural properties.¹¹² synthesized activated carbon via a single-step H₃PO₄ activation, followed by urea doping as an N₂ precursor and pyrolysis at 1000 °C. Carbonization was performed under N₂ at 550 °C for 1 hour with a heating rate of 10 °C/min, yielding a surface area of 1216 m² g⁻¹ and a pore volume of 1.15 cm³ g⁻¹ (72% yield). XPS analysis confirmed the presence of C_{1s} (284.3 eV), P_{2p} (133 eV), O_{1s} (532 eV), and N_{1s} (400 eV).¹¹⁴ evaluated protein adsorption using H₃PO₄-activated carbon derived from coconut shells. Carbonization under N₂ at 500 °C for 40 minutes produced activated carbon with a surface area of 642 m² g⁻¹. H₃PO₄ effectively modified the structure of precursor and carbon texture. Similarly,¹¹⁵

reported surface areas of 1737-1211 m² g⁻¹ at 400 °C, while cotton stalk-derived carbon exhibited surface areas of 330-1720 m² g⁻¹ and total pore volumes of 0.15-1.23 cm³ g⁻¹, with mesopore volumes of 0-0.61 cm³g⁻¹.⁶⁴ investigated H₃PO₄ co-carbonization of cellulose with lysine, melamine, chitosan, and dicyandiamide, achieving N contents of 2-12 wt%. XPS analysis identified dominant pyrolytic-N, including pyridinic-N (398.3 eV) and pyrrolic-N (400.2 eV). The addition of H₃PO₄ influenced lysine formation and increased the conversion rate to 78%. Its strong acidic behavior promoted mesopore formation by degrading the solid matrix, significantly enhancing porosity.

5.2.3. Carbonization followed by zinc chloride

Carbonization with N-doping followed by zinc chloride (ZnCl₂) activation has been employed to produce activated carbon from biomass, showing promising potential for energy storage applications.^{14, 110, 116-119} Table 4 provides data on the impact of ZnCl₂ activation on capacitance and surface area.¹¹⁰ investigated activated carbon derived from Enteromorpha clathrata using ZnCl₂ activation under an N₂ atmosphere. Samples were heated to 800 °C at a rate of 5 °C min⁻¹ and maintained for 60 minutes. The resulting surface area and pore volume for urea- and ZnCl₂ treated samples were 217.27 m² g⁻¹ and 0.327 cm³ g⁻¹, respectively

Table 4. Chemical activation of derived biomass with ZnCl₂

Nitrogen doping	Green materials	Synthesize methods	Carbonization (°C)	Surface areas (m ² g ⁻¹)	Functional groups	Ref.
NH ₃	Saw dust	Carbonization: 1 h Activation: N/A	600, 700, 800 125 (5°C min ⁻¹)	281.8–964.9	O–H, C–O, O–H, C=C, and C–N=C	¹¹⁶
Urea	Pomegranate husk	Carbonization: 2 h Activation: 24 h	800 (5°C min ⁻¹) 60	445–1755	Pyridinic-N, pyrrolic-N (N–5), quaternary-N (N–Q)	¹¹⁷
Urea	Jujube shell	Carbonization: 4 h Activation: N/A	900	-	C = O, C–H, C–N	¹¹⁸
Urea	Sugar cane bagasse	Carbonization: 2 h Activation: N/A	800	973–1506	C=C, pyridinic-N, pyrrolic-N, quaternary-N	¹²⁰
Urea	Citrus aurantium waste leaves	Carbonization: 8 h Activation: N/A	120	346–937	C-N, N-H, N-H	¹²¹

Urea combined with ZnCl₂ resulted in a surface area of 188.89 m²g⁻¹ and a pore volume of 0.30 cm³/g, while urea combined with KOH produced a surface area of 144.81 m²g⁻¹ with the same pore volume. Notably, all pore diameters remained consistent, ranging from 3.82 to 3.83 nm. ZnCl₂ demonstrated superior porous structure formation, aligning with¹²² findings that ZnCl₂ enhances pore development by acting as a structural scaffold during catalytic dehydration at high temperatures. Additionally, ZnCl₂ reacts with hydrogen and oxygen on the material's surface, forming H₂O and H₂.¹²³ The presence of ZnCl₂ also enhances C=N functional groups, while higher temperatures play a crucial role in interlinked pore formation.

Zinc ions disrupt the carbon skeleton, promoting internal pore development.^{124 125} reported that ZnCl₂ activated biomass from water hyacinth at 700 °C exhibited high concentrations of pyridinic, pyrrolic, and graphitic nitrogen, confirming excellent electrocatalytic activity. These findings highlight how different activation methods influence the functional groups within the material's framework. Furthermore,¹²⁶ utilized bio-oil from biomass thermal conversion to synthesize N-doped hierarchically porous carbon via one-step ZnCl₂ activation, achieving a surface area of 920.57 m²g⁻¹ and a large pore volume of 0.55 cm³/g. Mesopore and micropore volumes were measured at 0.385 cm³/g and 0.163 cm³g⁻¹, respectively, with



high porosity ranging from 86.28% to 91.56%. Functional groups identified included C=O, C=C, O-C=O, and C/C-N.¹²⁷ Overall, ZnCl₂ effectively enhances surface properties by introducing functional groups and facilitating a well-distributed mesoporous structure. It serves as a valuable activator for N-doped carbonization, with temperature regulation playing a key role in optimizing pore size distribution.

5.2.4. Activation using potassium carbonate

This section discusses N-doped carbonization followed by chemical activation using potassium carbonate (K₂CO₃).¹²⁸⁻¹³¹ ¹²⁹ prepared activated carbon from waste medium-density fiberboard, which contains aldehyde resin as an adhesive, for electrode material applications. XPS analysis identified nitrogen species within graphene layers, including N-6 (pyridinic N₂), N-5 (pyrrolic and pyridinic N₂), N-Q (quaternary N₂), and N-X (oxidized N₂). The surface area ranged from 817 to 1027 m²g⁻¹, with an average of 800 m²g⁻¹. The electrodes exhibited capacitances between 147 and 223 F g⁻¹ at a current density of 0.5 A g⁻¹. ¹³⁰ investigated activated carbon derived from coconut shells, modified with K₂CO₃ and urea. Activation was conducted at 600 °C for 1 hour under an N₂ flow rate of 400 mL min⁻¹, with a heating rate of 5 °C min⁻¹. The surface area of N-doped samples ranged from 947 to 1430 m²g⁻¹, while total pore volume and micropore volume were 0.35-0.65 cm³/g and 0.34-0.58 cm³ g⁻¹, respectively. Activation at 900 °C significantly increased micropore volume. The electric double-layer properties of K₂CO₃-activated carbon were influenced by carbonization and activation parameters, including temperature, duration, and K₂CO₃ concentration. Nitrogen content ranged from 0.93% to 2.86%, while the specific surface area and capacitance varied between 569-1027 m²g⁻¹ and 147-223 F g⁻¹, respectively. Additionally, ¹³² studied activated carbon derived from waste tea, investigating the effects of K₂CO₃ activation at different temperatures and durations. The highest surface area, 1722 m²g⁻¹, was achieved at 900 °C, surpassing other studies at lower temperatures. These findings confirm that K₂CO₃ activation plays a crucial role in enhancing porosity, with temperature optimization being a key factor in achieving high-performance materials.

5.3. Physical activation

Physical activation generally involves two stages: an initial carbonization step at 400-500 °C, followed by activation using steam or CO₂ at 900-1000 °C.¹³³ The activation temperature significantly influences the specific surface area, making physical activation a widely studied, cost-effective method. This process enhances adsorption capacity by developing a porous network in biochar, yielding specific surface areas between 1000-1500 m²g⁻¹ with a pore volume of less than 1 cm³g⁻¹.¹³⁴ Additionally, physical activation removes residual impurities from the pores formed during carbonization. The CO₂ reaction with carbon produces CO, CO₂, H₂, and CH₄, contributing to pore enlargement. However, physical activation has drawbacks,

including substantial mass loss, low mechanical strength, and limited carbon yield.⁹⁶ Despite these challenges, it is considered a cleaner alternative to chemical activation and remains a viable low-cost approach with high adsorption capacity and reduced weight loss.

Recent studies have explored N-doping followed by NH₃ activation of biomass to produce activated carbon, as summarized in Table 5. For example, ¹³⁵ synthesized activated carbon from pine sawdust via NH₃ activation at 700-900 °C for 2 hours. The activated material, mixed with conductive graphite and polyvinylidene fluoride (PVDF) in N-methyl-2-pyrrolidone (NMP) at an 8:1:1 ratio, was treated with NH₃ and air at controlled flow rates (NH₃: 100 mL/min; NH₃/air: 50 mL/min with 21% O₂). The specific surface area is 757 m²g⁻¹ and micropore volume of 0.42 cm³ g⁻¹. XRD analysis confirmed the presence of graphite-like carbon, while functional groups included C=O, C-C, C-O, O-H, and -NH. Similarly, ¹³⁶ developed activated carbon from Moso bamboo (*Phyllostachys edulis*) via NH₃ activation at 200-300 °C, followed by tube furnace heating at 450-750 °C. The resulting material exhibited N-functional groups (pyridinic-N, pyrrolic-N, and quaternary-N) and oxygen-containing groups (-C=O, C=OH, -COO-), with N-functional contributions exceeding 85%. NH radicals (NH*) played a key role in functionalization by reacting with bamboo-derived materials.

Sun, F., et al. heated 3 g of raw coal at 800 °C for 2 hours in an NH₃/N₂ mixture (1:1 ratio) at a heating rate of 5 °C min⁻¹.¹³⁷ The resulting carbon black, combined with polytetrafluoroethylene at an 8:1:1 ratio, the specific surface area and pore volume were 1235 m²g⁻¹ and 0.58 cm³g⁻¹, respectively, with functional groups including C-H, O-H, N-H, C-N, and C=O. ¹³⁸ pyrolyzed crop straw at 600 °C for 2 hours, replacing N₂ with NH₃ for N-doping at 600 °C for 1 hour, resulting in surface areas of 72.7-418.7 m²g⁻¹.

Physical activation involves low-temperature carbonization (600 °C) followed by high-temperature activation (800-900 °C). The interaction of high-temperature gases with the material promotes pore formation, while water vapor, CO₂, and other gases contribute to structural stability. These processes highlight the role of physical activation in developing high-performance porous carbon materials.

Prauchner et al. activated coconut shells using CO₂,⁹⁶ first heating them under N₂ at 850 °C for 2 hours, followed by carbonization at 750 °C with CO₂. This process resulted in narrow pores (<0.7 nm) and 3% CO₂ saturation at 0 °C. Physical activation involves gas diffusion into the carbon material's pores, leading to surface reactions. Temperature and CO₂ flow rate have a significant impact on surface properties, affecting both electrical conductivity and pore structure. While chemical activation produces larger surface areas, both physical and chemical activation influence pore distribution and electronic properties, enhancing performance in energy storage applications like Li-ion batteries and fuel cells.



Table 5. Physical activations of synthesized material via N-doping methods

N-doping	Physical activation	Precursor	Synthesis methods	Carbonization (°C)	Surface areas (m ² g ⁻¹)	Functional Groups	Ref.
NH ₃	Air oxidation	Pine sawdust	Carbonization: 12 h Activation: N/A	700, 800, 900	757	C=O, C–O, C–N and C=C, pyridinic-N (N-6), pyrrolic-N (N-5), quaternary-N (N-Q), and oxidized-N (N-X).	135
NH ₃	NH ₃ (Torrefaction)	Moso bamboo (<i>Phyllostachys edulis</i>)	Carbonization: 12 h Activation: N/A	450, 550, 650, and 750 200, 250, and 300	N/A	–COO–, –C=O, C–OH	136
NH ₃	NH ₃	Crop straw	Carbonization: 3 h Activation: 2–3 h	600, 700 and 800	72.70 (600°C) to 418.70 (800 °C).	pyridine-N, pyrrolic/pyridone-N, and oxidized-N.	138
Urea	CO ₂	Coconut leaf	Carbonization: 3 h Activation: 1 h	700 800	419	C=C, C–OH, C=O, C=O, C–OH, and C–O–C	40
N/A	CO ₂	Bean pulp	Carbonization: 3 h Activation: 1 h	800	558.20	O–C, C=O, –C–N, N–H, C–O, C=O, C–O–C, Pyridinic N, Pyridinic N, graphitic N, oxidized N	139
N/A	CO ₂	Water-caltrop shell	Carbonization: 2 h Activation: 3 h	750 800 - 950	N/A	graphitic-N, oxidized-N, graphitic-N	140
NH ₃	Steam	Bamboo charcoal	Carbonization: 120 min	600 850-950	2032	pyridinic-N, pyrroline-N atoms, quaternary-N, N-oxides	141
Urea	Water steam	Peach stones	Carbonization: 30 min	550, 700-750	846	N/A	142

According to the review above regarding to the chemical and physical activation, we have concluded the key points below: Ammonoxidation with Alkaline Activation (KOH) is highly efficient in creating high specific surface areas (up to 2995 m²g⁻¹) and well-developed porous structures, which are crucial for supercapacitor applications. The method also introduces functional groups like C=O, C–O–C, and C–O–H, which enhance electrochemical capacitance through faradic reactions. While KOH activation requires high temperatures (700–900 °C), which can lead to a decrease in micropore percentage at higher temperatures. This trade-off between surface area and pore size distribution needs to be carefully managed depending on the application. Activation using Sodium Carbonate (Na₂CO₃) is less aggressive compared to KOH, resulting in lower surface areas (up to 1148 m²g⁻¹) but with a higher nitrogen content (up to 13.1 wt%). The lower surface area compared to KOH

activation may limit its use in applications requiring high surface area. However, the higher nitrogen content can be advantageous for specific electrochemical applications where redox activity is more critical than surface area. Activation using Orthophosphoric Acid (H₃PO₄) is effective in creating mesoporous structures with surface areas ranging from 330 to 1720 m²g⁻¹. It also introduces phosphorus and nitrogen functional groups, which can enhance the electrochemical performance. H₃PO₄ activation is particularly useful for creating mesopores, which are beneficial for electrolyte penetration and ion transport. However, the surface areas are generally lower than those achieved with KOH activation, making it less suitable for applications requiring very high surface areas. Activation using Zinc Chloride (ZnCl₂) is effective in creating a well-developed pore structure with surface areas up to 1755 m²g⁻¹. It also introduces nitrogen functional groups, which are



beneficial for electrochemical applications. ZnCl_2 activation is comparable to KOH in terms of surface area and pore structure development. However, it may require careful control of temperature to avoid excessive pore widening, which can reduce the material's effectiveness in certain applications. Activation using Potassium Carbonate (K_2CO_3) can produce surface areas up to $1430 \text{ m}^2\text{g}^{-1}$ and introduces nitrogen functional groups. It is effective in creating microporous structures, which are beneficial for high capacitance. K_2CO_3 activation is less aggressive than KOH, resulting in lower surface areas but with better control over pore size distribution. This makes it suitable for applications where a balance between surface area and pore size is critical.

Physical Activation (CO_2 , Steam): Physical activation methods, such as CO_2 and steam activation, can produce surface areas up to $2032 \text{ m}^2\text{g}^{-1}$. These methods are cleaner and lower cost compared to chemical activation but generally result in lower surface areas and less control over pore structure. Physical activation is less efficient in creating high surface areas compared to chemical activation methods. However, it is more environmentally friendly and cost-effective, making it suitable for large-scale applications where high surface area is not the primary requirement. CO_2 activation is effective in creating narrow pores (less than 0.7 nm) and can produce surface areas up to $850 \text{ m}^2\text{g}^{-1}$. It is particularly useful for creating microporous structures. CO_2 activation is less efficient in creating high surface areas compared to chemical activation methods. However, it is useful for applications requiring narrow pores and is more environmentally friendly.

As concluded above, we have obtained that KOH and ZnCl_2 activations are the most efficient in creating high surface areas, making them suitable for supercapacitor applications where high surface area is critical. While H_3PO_4 and ZnCl_2 activations are effective in creating mesoporous structures, which are beneficial for electrolyte penetration and ion transport. Physical activation methods (CO_2 , steam) are more environmentally friendly and cost-effective but generally result in lower surface

areas and less control over pore structure. The choice of activation method depends on the specific requirements of the application. Future studies should focus on optimizing these methods to balance surface area, pore structure, and functional group introduction for specific applications.

5.4. AI-assisted preparation of nitrogen-doped biochar

Recent advancements in artificial intelligence (AI) have significantly contributed to the optimization of nitrogen-doped (N-doped) biochar materials for energy storage applications. Machine learning (ML) techniques, such as Random Forest (RF)¹⁴³ and Extreme Gradient Boosting (XGBoost)¹⁴⁴, have been employed to predict the specific capacitance of N-doped biochar as displayed in . These models utilize a comprehensive set of features, including pore structure parameters, elemental composition, N-containing functional groups, and electrochemical testing characteristics. To better understand how these features influence capacitance, Shapley additive explanations and partial dependency plots were applied. The results demonstrated exceptional predictive performance, with R^2 values of 0.95 for RF and 0.96 for XGBoost. Notably, among the three N-containing groups, N-6 was identified as the most significant contributor to higher specific capacitance. Partial dependency plot analysis further revealed that optimal conditions for enhanced capacitive performance occur when the specific surface area is approximately $2200 \text{ m}^2\text{g}^{-1}$, the pore size is around 4 nm , and the degree of graphitization is about one. Beyond traditional ML approaches, deep learning models have also been explored for biochar characterization. A Convolutional Neural Network (CNN) based on the DenseNet architecture was developed to enhance predictive accuracy. The CNN model consisted of an input layer and two hidden layers employing the ReLU (Rectified Linear Unit) activation function to introduce non-linearity, enabling the model to learn complex patterns efficiently. This approach allows for advanced feature extraction, leveraging DenseNet's strength in improving model performance.

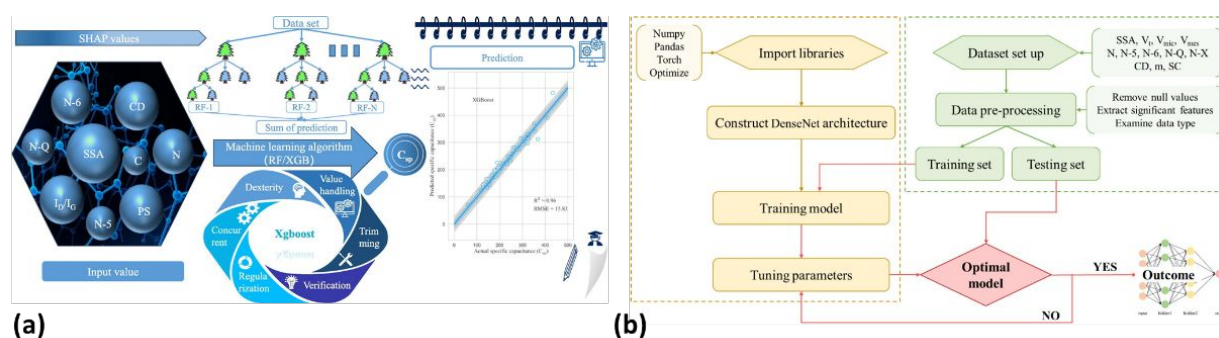


Fig. 5 (a) Machine learning prediction of supercapacitor performance of N-doped biochar from biomass wastes based on N-containing groups, element compositions, and pore structures. (b) Workflow of the Convolutional Neural Network modeling process of nitrogen-doped porous biochar.



Review

6. Density functional theory (DFT) of N-doping materials

DFT plays a crucial role in elucidating the relationship between N-doping and carbon materials by enabling the calculation of structural and interfacial characteristics governing adsorbent–molecule interactions^{76, 145, 146} and usually focused on formation of energy and chemical potential (μ) associated of pyridinic-N and pyrrolic-N¹⁴⁷. Mostly, the surface contains of —OH, and —COOH, and appears as —COOH, —OH, and —NH₂¹⁴⁸, and sometimes overlapped of O — H at N — H, which is exist in materials¹⁴⁸. It is associated with electrostatic and hydrogen-bonding interaction, with π — π , electrostatic, and H₂ interactions. DFT calculation results confirmed that pyridinic — N species for N-doping carbon materials is associated with the CO₂RR¹⁴⁹. Interactions of the chemical or targets with MNB include π — π , electrostatic, and hydrogen bonding interactions. Generally, the formation energy of pyridinic-N is lower than graphene at N-rich conditions, which indicated that hybrid is more beneficial for obtaining active pyridinic-N sites. Electrons of pyridinic-N play a major role to release the *COOH intermediate, where it enhances the CO₂RR catalytic activity, containing of active origin pyridinic-N sites¹⁵⁰. Also, pyrrolic nitrogen plays a pivotal role to improve the capacitance of materials, especially for the supercapacitors. In terms of graphitic-N, it improves the quantum capacitance. Conversely, pyrolytic improvement is associated with total capacitance because of its lower quantum capacitance¹⁵¹. From this point of view, controlling the type and concentration of N-Doping is suggested during the carbonization and activation because higher total quantum capacitance has a direct impact towards total capacitance, as suggested by¹⁵¹ that controlling in order to optimize the capacitance, it can be performed by the type and concentration of N-Doping. In further analysis of some scholar, calculation of DFT will give an important information

related to structure of the material itself precisely, where it should be referred to proper control of types and concentration of N-Doping¹⁵².

Table 6 identifies the fitted peaks of parameters from the XPS that associated with the functional groups from N-Doping activation. N1s, in different peaks formation, represents existence of Pyridinic N, Pyrrolic N, Pyridinic-N-oxide, Graphitic N, and Quaternary N, as the result of N-Doping carbonization. Mostly, N-rich carbon materials, which is synthesized via nitridizing carbon precursor or direct N-containing materials, have a contribution of N and multi-species, such as N-5, N-6t, N-Q and N-X). The existence of N species provides the electron donors on the carbon layers, confirming the electrochemical carbon and active sites on the pseudocapacitive reactions, for the electrochemical storage applications. Moreover, the presence of N-species indicates a greater electrochemical performance. As a result, the combination of capacitance and pseudocapacitance have an impact towards the largest specific capacitances in material itself^{153, 154} also demonstrated that pyridinic nitrogen improves the capacitance related to the material design and synthesis. Furthermore, N-Doping improves more active sites, O₂ vacancies, high surface area, and morphology. It provides the effect of N₂ associated on the electronic properties, catalytic activity, reaction mechanism and stabilization of N-Doping carbon. In this case, characterization of materials via the XPS to identify peaks of the parameters associated with the assignment. Different formations of porous structure in different biomass exist with different porous structures, depending on the treatment of biomass itself as a result of N-Doping treatment. Thus, it is clear that the N-Doping presences the different characteristics of materials for the energy storage applications

Table 6. Fitted of peaks parameters from XPS that assignment to elemental composition in surface material from the N-doping activation

Elements	Precursor	E _g (eV)	Assignments	Ref.
N1s	Soybean	398.5	pyridine-N	15
N1s	Soybean	401.2	graphitic-N	15
N1s	Corncob	398.1	pyridine-N	109
N1s	Corncob	399.4	Ph-NH ₂	109
N1s	Sugar cane bagasse	398.2	pyridinic-N (N-6)	14
N1s	Sugar cane bagasse	399.7	pyrrolic N (N-5)	14
N1s	Sugar cane bagasse	401.2	quaternary N (N-Q)	14
N1s	Sugar cane bagasse	403.0	oxidized nitrogen atoms (N-X)	14
N1s	Tamarind shell	401.5	pyridine N	12



N1s	Tamarind shell	404.2	pyrrole-like Nitrogen	12	View Article Online DOI: 10.1039/D5SU00555H
N1s	Licorice root	398.4	pyridinic-N (N-6)	17	
N1s	Licorice root	400.7	pyrrolic N (N-5)	17	
N1s	Licorice root	401.5	quaternary N (N-Q)	17	
N1s	Licorice root	402.9	pyridinic-N-oxide (N-6)	17	
N1s	Water hyacinth	401.2	Graphitic N	125	
N1s	Water hyacinth	399.2	Pyrrolic N	125	
N1s	Water hyacinth	398.4	Pyridinic N	125	

The DFT calculations demonstrate that nitrogen-doping, particularly pyridinic-N and pyrrolic-N in carbon materials, significantly enhances the adsorption ability of potassium ions, leading to improved potassium-storage performance.¹⁵⁵ Three N-doping models-N-5, N-6, and NQ-were analyzed by placing potassium atoms at different positions in each model to calculate adsorption energies. The results showed that the ΔE_a values of N-5 (-2.63 eV) and N-6 (-2.86 eV) were higher than that of NQ (0.14 eV), indicating that pyrrole and pyridine N-doping enhance potassium adsorption capacity more than graphite N-doping.¹⁵⁶ Among the models, N-6 doping exhibited the lowest ΔE_a , with the highest electron density and consequently a greater K^+ adsorption capacity. This capacity was further enhanced with an increase in N-doping content. Additionally, N-doping improves the electrochemical properties and performance of hard carbon materials. Nitrogen-doping configurations like pyridinic-N, pyrrolic-N, and graphitic-N have distinct effects on K-ion absorption and migration, which ultimately affect the overall performance of the materials. DFT simulations of N-doped graphene show enhanced properties for supercapacitors when graphene is doped with graphite, pyrrole, or pyridine nitrogen.¹⁵⁷ N-doping also helps reduce volume expansion during the simulation process, which is typically responsible for poor cell performance, as indicated by DFT results. In the context of CO_2 capture, DFT calculations also reveal that nitrogen-doped carbon materials exhibit significantly higher CO_2 adsorption compared to pristine carbon. Nitrogen-doping alters the local charge distribution and density of states (DOS), improving CO_2 adsorption performance. Specifically, the CO_2 adsorption energies for N-6 (G P-N 6), N-5 (G P-N 5), and NQ (G P-N Q) were calculated as -2.57 eV, -1.79 eV, and -0.28 eV, respectively. This shows that G P-N 6 and G P-N 5 have a stronger tendency to adsorb CO_2 . N-doping increases the dispersion and electrostatic interactions between CO_2 and biochar, with higher nitrogen content leading to a more pronounced improvement in adsorption performance.¹⁵⁸

7. Challenges, Perspectives, and Future Prospects of N-Doped Green Materials

The development of nitrogen-doped (N-doped) green materials holds immense promise, yet several technical challenges persist. One major challenge lies in optimizing the nitrogen content while preserving the structural integrity of the carbon framework. A delicate balance must be achieved excess nitrogen can weaken the carbon network, while insufficient

doping reduces the number of electrochemically active sites, ultimately impacting specific capacitance and performance. Additionally, thermal instability during high-temperature chemical activation, such as KOH treatment, often results in nitrogen volatilization, diminishing the overall nitrogen content and associated functionalities. Another critical challenge is controlling porosity and pore size distribution. The electrochemical performance and CO_2 adsorption capacity of these materials strongly depends on a well-developed and hierarchical pore structure. However, precisely tailoring the balance between micropores, which enhance adsorption, and mesopores, which facilitate ion transport, remains difficult. Furthermore, transitioning from lab-scale synthesis to industrial production is hindered by scalability and cost-efficiency concerns. High energy inputs and expensive activating agents pose obstacles to the economic viability of these materials. In capacitive deionization (CDI) applications, a trade-off exists between ion storage and mobility-micropores improve ion adsorption but limit transport, whereas mesopores offer enhanced diffusion but may compromise capacity. Achieving an optimal pore architecture for CDI performance is therefore essential.

Despite these challenges, promising perspectives emerge for advancing N-doped biomass-derived materials. Biomass offers an abundant, low-cost, and sustainable precursor for producing functional carbon materials suitable for energy storage, CO_2 capture, and CDI. The introduction of nitrogen-rich compounds such as urea during synthesis has shown to enhance nitrogen retention and improve the resulting material's electrochemical behavior. Modifying activation conditions—such as temperature and time also allows for tuning pore structure and maximizing specific capacitance. Nitrogen configurations like pyridinic-N, pyrrolic-N, and graphitic-N have been identified as key contributors to enhanced conductivity, charge storage, and redox activity, while oxygen-containing groups (e.g., C=O and C-O) further contribute to capacitive behavior. Controlling the activation temperature is especially crucial. For instance, thermal treatment in the range of 700–900 °C is often optimal for achieving high surface areas, mesoporous structures, and desirable C/O ratios. Chemical activation, particularly with KOH, can yield specific surface areas exceeding 2900 m²/g, significantly enhancing electrochemical and adsorption performance.

Looking ahead, several future prospects are expected to shape the evolution of N-doped green materials. Research into advanced modification strategies, including dual or tri-doping with heteroatoms such as sulfur, phosphorus, or boron, could lead to synergistic effects that boost material performance.



Furthermore, developing scalable, energy-efficient, and low-cost synthesis routes is essential for commercial deployment in applications like supercapacitors, lithium-ion batteries, and CO₂ capture systems. The integration of N-doped materials with emerging technologies including hybrid capacitors, metal-air batteries, and next-generation energy storage platforms offers exciting opportunities for multifunctional and high-efficiency devices. Additionally, expanding the range of biomass precursors beyond traditional sources to include algae, agricultural waste, and industrial by-products may further enable the tailoring of pore structure, conductivity, and surface chemistry for specific application demands. These advancements will be instrumental in bridging the gap between lab innovation and real-world impact, aligning green material development with global sustainability goals

8. Conclusion

In this review, the synthesis of N-doping from especially plants has been explored to understand its process and results, involving pre-carbonization, carbonization followed by activation through chemical and physical methods to adjust its surface area, functional groups and specific kind of N-doping. Various carbonization and activation methods, including chemical and physical activation, have a direct impact on surface materials. The presence of pyridinic N, graphitic N, and oxidized N in the material confirms the role of N₂ in material carbonization. After carbonization using different activation methods, functional groups such as C=O, C–C, C–O, C–N, C–H, C–O–C, C–H, –OH, graphitic N, pyrrolic N, pyridinic N, and quaternary N are observed in the material. However, the resulting surface area and capacitances vary significantly for energy storage applications. Porous N-doping derived from biomass enhances activated porous carbon by increasing surface area and enhancing electrochemical catalytic reactions, providing more active sites and electronic conductivity for energy storage applications. The electrocatalytic activity, particularly oxygen reduction reaction (ORR), is associated with the presence of N functional groups in the materials.

Chemical activation using KOH is widely used to create surface area. Additionally, DFT calculations are recommended to determine the structure and characteristics of molecules in the materials, confirming electrostatic and hydrogen bonding interactions. Future research on N-doping porous carbons should focus on DFT analysis, especially post-carbonisation and post-activation methods, to obtain crucial information for material design. Recycling methods for the material itself should be studied to assess quality. Plasma treatments further investigate surface areas of biomass-derived materials post-treatment, considering additional chemical and physical activation methods for further utilization. Additionally, expanding material applications beyond energy storage to include CO₂ adsorption, CDI, and battery applications is recommended.

CRedit authorship contribution statement

Xiang-Mao Huang: Methodology, Software, Formal analysis, Investigation, Data curation, Visualization, Validation, Investigation, Writing - Original Draft. **Mengyao Gao:** Conceptualization, Methodology, Writing - Original Draft, Writing - Review & Editing, Supervision, Project administration, Funding acquisition. **Dessie Ashagrie Tafere:** Writing - Review & Editing, Data Curation, Methodology, Formal analysis. **Shao-Yu Wang:** Writing - Original Draft, **Luthfiyyah Annisa Nur Azizah,** Writing - Original Draft, Visualization. **Yan-Ling Yang:** Investigation.

Conflicts of interest

There are no conflicts to declare.

Data availability

No primary research results, software or code have been included and no new data were generated or analysed as part of this review.

Acknowledgements

This work was supported by the National Science and Technology Council (NSTC) of Taiwan ROC under Grants number NSTC 113-2221-E-011-145, NSTC 114-2221-E-011 -118 -.

References

1. N. K. Arora and I. Mishra, *Environmental Sustainability*, 2022, **5**, 395-399.
2. T. Khandaker, T. Islam, A. Nandi, M. A. A. M. Anik, M. S. Hossain, M. K. Hasan and M. S. Hossain, *Sustainable Energy & Fuels*, 2025, **9**, 693-723.
3. J. Mu, S. I. Wong, Q. Li, P. Zhou, J. Zhou, Y. Zhao, J. Sunarso and S. Zhuo, *Journal of Alloys and Compounds*, 2020, **832**.
4. L. Qin, Z. Zhou, J. Dai, P. Ma, H. Zhao, J. He, A. Xie, C. Li and Y. Yan, *Journal of the Taiwan Institute of Chemical Engineers*, 2016, **62**, 228-238.
5. A. K. Mondal, K. Kretschmer, Y. Zhao, H. Liu, H. Fan and G. Wang, *Microporous and Mesoporous Materials*, 2017, **246**, 72-80.
6. Y. Deng, J. Chen, Z. Xiao, J. Liu, J. Zhang, B. Zhu, X. You, F. Ni, T. Ao and Y. Tan, *Water, Air, & Soil Pollution*, 2024, **235**.
7. L. Feng, X. Li, X. Chen, Y. Huang, K. Peng, Y. Huang, Y. Yan and Y. Chen, *Sci Total Environ*, 2020, **708**, 135071.
8. T. Liamprawat, P. Verasarut, N. Kaewtrakulchai, G. Panomsuwan, M. Fuji and A. Eiad-Ua, *Materials Science Forum*, 2020, **990**, 155-160.
9. B. Yang, J. Gao, M. Xie, S. Zuo, H. Kang, Y. Sun, X. Xu, W. Wang, C. Gao, Y. Liu and J. Yan, *J Colloid Interface Sci*, 2020, **579**, 832-841.
10. M. Gao, C.-C. Shih, S.-Y. Pan, C.-C. Chueh and W.-C. Chen, *Journal of Materials Chemistry A*, 2018, **6**, 20546-20563.



11. K. Xiao, H. Liu, Y. Li, G. Yang, Y. Wang and H. Yao, *Chemical Engineering Journal*, 2020, **382**.
12. V. Muthukumaraswamy Rangaraj, A. Achazhiyath Edathil, Y. Y. Kannangara, J.-K. Song, M. Abu Haija and F. Banat, *Journal of Electroanalytical Chemistry*, 2019, **848**.
13. S. Shi and Y. Liu, *Fuel*, 2021, **306**.
14. K. Zou, Y. Deng, J. Chen, Y. Qian, Y. Yang, Y. Li and G. Chen, *Journal of Power Sources*, 2018, **378**, 579-588.
15. G. Lin, R. Ma, Y. Zhou, Q. Liu, X. Dong and J. Wang, *Electrochimica Acta*, 2018, **261**, 49-57.
16. A. J. C. Mary, C. Nandhini and A. C. Bose, *Materials Letters*, 2019, **256**.
17. J. Gao, D. Fan and X. Liu, *New Journal of Chemistry*, 2021, **45**, 15469-15474.
18. Z. Bi, Q. Kong, Y. Cao, G. Sun, F. Su, X. Wei, X. Li, A. Ahmad, L. Xie and C.-M. Chen, *Journal of Materials Chemistry A*, 2019, **7**, 16028-16045.
19. D. Song, J. Yu, M. Wang, Q. Tan, K. Liu and J. Li, *Energy Storage Materials*, 2023, **61**.
20. S. Chawla, P. Rai, T. Garain, S. Uday and C. M. Hussain, *Trends in Environmental Analytical Chemistry*, 2022, **33**.
21. C. P. T. Devatha, Arun K., in *Synthesis of Inorganic Nanomaterials*, 2018, DOI: 10.1016/b978-0-08-101975-7.00007-5, pp. 169-184.
22. S. Kumar, G. Saeed, L. Zhu, K. N. Hui, N. H. Kim and J. H. Lee, *Chemical Engineering Journal*, 2021, **403**.
23. N. Yan and X. Chen, *Nature*, 2015, **524**, 155-157.
24. P. Liu, Y. Wang and J. Liu, *Journal of Energy Chemistry*, 2019, **34**, 171-185.
25. S. S. Sekhon, P. Kaur and J.-S. Park, *Renewable and Sustainable Energy Reviews*, 2021, **147**.
26. P. Feng, J. Li, H. Wang and Z. Xu, *ACS Omega*, 2020, **5**, 24064-24072.
27. Y. Deng, Y. Xie, K. Zou and X. Ji, *Journal of Materials Chemistry A*, 2016, **4**, 1144-1173.
28. L. Dai, Y. Xue, L. Qu, H. J. Choi and J. B. Baek, *Chem Rev*, 2015, **115**, 4823-4892.
29. J. H. Hou, Cao, C.B., Idrees, F., Ma, X.L., , 2015 **9**, 2556-2564
30. F. Rodriguez-Reinoso, Molina-Sabio, M., , *Carbon* 1992 **30** 1111-1118.
31. N. Mohamad Nor, L. C. Lau, K. T. Lee and A. R. Mohamed, *Journal of Environmental Chemical Engineering*, 2013, **1**, 658-666.
32. P. González-García, *Renewable and Sustainable Energy Reviews*, 2018, **82**, 1393-1414.
33. R. C. Sanito, C. Lidwina, H. H. Yang and Y. F. Wang, *Heliyon*, 2022b, **8**, e11240.
34. M. Danish and T. Ahmad, *Renewable and Sustainable Energy Reviews*, 2018, **87**, 1-21.
35. M. A. Yahya, Z. Al-Qodah and C. W. Z. Ngah, *Renewable and Sustainable Energy Reviews*, 2015, **46**, 218-235.
36. K. Ukanwa, K. Patchigolla, R. Sakrabani, E. Anthony and S. Mandavgane, *Sustainability*, 2019, **11**.
37. O. Ioannidou and A. Zabanitout, *Renewable and Sustainable Energy Reviews*, 2007, **11**, 1966-2005. DOI: 10.1039/D5SU00555H
38. M. A. Yahya, M. H. Mansor, W. A. A. W. Zolkarnaini, N. S. Rusli, A. Aminuddin, K. Mohamad, F. A. M. Sabhan, A. A. A. Atik and L. N. Ozair, 2018.
39. S. V. Vassilev, D. Baxter, L. K. Andersen and C. G. Vassileva, *Fuel*, 2010, **89**, 913-933.
40. S. Wang, Z. Ren, J. Li, Y. Ren, L. Zhao and J. Yu, *RSC Adv.*, 2014, **4**, 31300-31307.
41. J. J. Lado, R. L. Zornitta, I. Vázquez Rodríguez, K. Malverdi Barcelos and L. A. M. Ruotolo, *ACS Sustainable Chemistry & Engineering*, 2019, **7**, 18992-19004.
42. L. Sun, Y. Gong, D. Li and C. Pan, *Green Chemistry*, 2022, **24**, 3864-3894.
43. C. Ruan, K. Ai and L. Lu, *RSC Advances*, 2014, **4**.
44. G. Ma, Q. Yang, K. Sun, H. Peng, F. Ran, X. Zhao and Z. Lei, *Bioresour Technol*, 2015, **197**, 137-142.
45. C. O. Ania, V. Khomenko, E. Raymundo-Piñero, J. B. Parra and F. Béguin, *Advanced Functional Materials*, 2007, **17**, 1828-1836.
46. D. Hulicova, Kodama, M., Hatori, H., , *Chem Matter* 2006 **18** 2318-2326
47. B. T. Liu, X. M. Shi, X. Y. Lang, L. Gu, Z. Wen, M. Zhao and Q. Jiang, *Nat Commun*, 2018, **9**, 1375.
48. T. Brousse, D. Bélanger and J. W. Long, *Journal of The Electrochemical Society*, 2015, **162**, A5185-A5189.
49. M. Zgrzebnicki, V. Nair, S. Mitra, A. Kałamaga, J. Przepiórski and R. J. Wrobel, *Chemical Engineering Journal*, 2022, **427**.
50. C. L. Mangun, Benak, K.R., Economy, J., Foster, K.L., , *Carbon*, 2001, **39**, 1809-1820.
51. Z. Wan, Y. Sun, D. C. W. Tsang, E. Khan, A. C. K. Yip, Y. H. Ng, J. Rinklebe and Y. S. Ok, *Chemical Engineering Journal*, 2020, **401**.
52. M. Nandi, K. Okada, A. Dutta, A. Bhaumik, J. Maruyama, D. Derks and H. Uyama, *Chem Commun (Camb)*, 2012, **48**, 10283-10285.
53. M. Li, C. Liu, H. Cao, H. Zhao, Y. Zhang and Z. Fan, *Journal of Materials Chemistry A*, 2014, **2**.
54. Y. Gao, W. Gao, H. Zhu, H. Chen, S. Yan, M. Zhao, H. Sun, J. Zhang and S. Zhang, *Int J Environ Res Public Health*, 2022, **19**.
55. A. Ilnicka, M. Skorupska, M. Szkoda, Z. Zarach and J. P. Lukaszewicz, *Materials Research Letters*, 2022, **11**, 213-221.
56. J. Hu, Z. Li, A. Zhang, S. Mao, I. R. Jenkinson and W. Tao, *Environ Res*, 2020, **188**, 109764.
57. W. Mao, J. Wang, Z. Xu, Z. Niu and J. Zhang, *Electrochemistry Communications*, 2006, **8**, 1326-1330.
58. J. He, D. Zhang, Y. Wang, J. Zhang, B. Yang, H. Shi, K. Wang and Y. Wang, *Applied Surface Science*, 2020, **515**.
59. Y. Zhou, S. Liu, Y. Liu, X. Tan, N. Liu and J. Wen, *Int J Environ Res Public Health*, 2020, **17**.
60. C. Yan, L. Zhu, J. Dong, D. Gu, H. Jiang and B. Wang, *R Soc Open Sci*, 2019, **6**, 180919.
61. K. Ö. Köse, B. Pişkin and M. K. Aydınol, *International Journal of Hydrogen Energy*, 2018, **43**, 18607-18616.



62. P. E. Hock and M. A. A. Zaini, *Acta Chimica Slovaca*, 2018, **11**, 99-106.
63. F. Cesano, S. Cravanzola, V. Brunella and D. Scarano, *Microporous and Mesoporous Materials*, 2019, **288**.
64. K. Mainali and M. Garcia-Perez, *Journal of Analytical and Applied Pyrolysis*, 2023, **169**.
65. P. Zhao, Y. Shen, S. Ge, Z. Chen and K. Yoshikawa, *Applied Energy*, 2014, **131**, 345-367.
66. S. M. Yakout and G. Sharaf El-Deen, *Arabian Journal of Chemistry*, 2016, **9**, S1155-S1162.
67. H. Demiral and I. Uzun, *Surface and Interface Analysis*, 2010, **42**, 1338-1341.
68. F. H. Emamy, A. Bumajdad and J. P. Lukaszewicz, *Nanomaterials (Basel)*, 2021, **11**.
69. T. E. Brown, H. E. LeMay, B. E. Bursten, C. Murphy, P. Woodward and M. E. Stoltzfus, *Chemistry: The Central Science in SI Units, Global Edition*, Pearson Education, 2021.
70. H. Wang, Y. Shao, S. Mei, Y. Lu, M. Zhang, J.-k. Sun, K. Matyjaszewski, M. Antonietti and J. Yuan, *Chemical Reviews*, 2020, **120**, 9363-9419.
71. Y. Ren, C. Yu, X. Tan, Q. Wei, Z. Wang, L. Ni, L. Wang and J. Qiu, *Energy & Environmental Science*, 2022, **15**, 2776-2805.
72. J. Lefebvre, J. Ding, Z. Li, P. Finnie, G. Lopinski and P. R. Malenfant, *Accounts of chemical research*, 2017, **50**, 2479-2486.
73. C. Wang, H. Dong, L. Jiang and W. Hu, *Chemical Society Reviews*, 2018, **47**, 422-500.
74. C.-X. Zhou, J.-X. Sun, Z.-J. Deng and S. Zhou, *Semiconductors*, 2013, **47**, 1351-1357.
75. M. A. Zazycki, P. A. Borba, R. N. F. Silva, E. C. Peres, D. Perondi, G. C. Collazzo and G. L. Dotto, *Advanced Powder Technology*, 2019, **30**, 1494-1503.
76. D. Adekoya, S. Qian, X. Gu, W. Wen, D. Li, J. Ma and S. Zhang, *Nanomicro Lett*, 2020, **13**, 13.
77. H. Miao, S. Li, Z. Wang, S. Sun, M. Kuang, Z. Liu and J. Yuan, *International Journal of Hydrogen Energy*, 2017, **42**, 28298-28308.
78. S. N. Faisal, E. Haque, N. Noorbehesht, W. Zhang, A. T. Harris, Tamara L. Church and A. I. Minett, *RSC Advances*, 2017, **7**, 17950-17958.
79. C. Falco, J. P. Marco-Lozar, D. Salinas-Torres, E. Morallon, D. Cazorla-Amorós, M.-M. Titirici and D. Lozano-Castello, *Carbon*, 2013, **62**, 346-355.
80. B. Sajjadi, W.-Y. Chen and N. O. Egiebor, *Reviews in Chemical Engineering*, 2019, **35**, 735-776.
81. B. Viswanathan, P. I. Neel and T. Varadarajan, *India, Chennai*, 2009, **600**, 1-160.
82. M. Kodama, J. Yamashita, Y. Soneda, H. Hatori, S. Nishimura and K. Kamegawa, *Materials Science and Engineering: B*, 2004, **108**, 156-161.
83. J. S. Noh, Schwarz, J.A., , *Carbon* 1990, **28** 675-682
84. K. Kaneko, Katori, T., Shimizu, K., Shindo, N., Maeda, T., , *J. Chem. Soc Faraday Trans.*, 1992 **88**, 1305-1309
85. B. A. Bashkova S, Badosz TJ, *Langmuir*, 2003 **19**, 6115-6121.
86. A. Bagreev, J. Angel Menendez, I. Dukhno, Y. Tarasenko and T. J. Badosz, *Carbon*, 2004, **42**, 469-476 DOI: 10.1039/D5SU00555H
87. F. Adib, Bagreev, A., Badosz, T.J., , *Langmuir* 2000, **16** 1980-1986
88. W. Chen, F. S. Cannon and J. R. Rangel-Mendez, *Carbon*, 2005, **43**, 573-580.
89. M. Abe, Kawashima, K., Kozawa, K., Sakai, H., Kaneko, K., , *Langmuir*, , 2006 5059-5063
90. M. Seredych, D. Hulicova-Jurcakova, G. Q. Lu and T. J. Badosz, *Carbon*, 2008, **46**, 1475-1488.
91. J. Lahaye, Nanse, G., Bagreev, A., Strelko, V., , *Carbon* 1999 **37**, 585-590
92. V. V. Strelko, Kuts, V.S., Thrower, P.A., , *Carbon* 2000, **38** 1499-1524
93. B. Stohr B, H.P., Schlogl, R., , *Carbon*, 1991 **29**, 707-720.
94. L. Yan, J. Yu, J. Houston, N. Flores and H. Luo, *Green Energy & Environment*, 2017, **2**, 84-99.
95. Z. Chen, S. Yun, L. Wu, J. Zhang, X. Shi, W. Wei, Y. Liu, R. Zheng, N. Han and B.-J. Ni, *Nano-Micro Letters*, 2023, **15**, 4.
96. M. J. Prauchner and F. Rodríguez-Reinoso, *Microporous and Mesoporous Materials*, 2012, **152**, 163-171.
97. A. R. Mohamed, M. Mohammadi and G. N. Darzi, *Renewable and Sustainable Energy Reviews*, 2010, **14**, 1591-1599.
98. X. Yang, T. Lv and J. Qiu, *Small*, 2023, **19**, e2300336.
99. J. Zhou, P. Yang, P. A. Kots, M. Cohen, Y. Chen, C. M. Quinn, M. D. de Mello, J. Anibal Boscoboinik, W. J. Shaw and S. Caratzoulas, *Nature communications*, 2023, **14**, 2293.
100. L. Guo, J. Yang, G. Hu, X. Hu, L. Wang, Y. Dong, H. DaCosta and M. Fan, *ACS Sustainable Chemistry & Engineering*, 2016, **4**, 2806-2813.
101. J. Wang and S. Kaskel, *Journal of Materials Chemistry*, 2012, **22**.
102. J. M. Dias, M. C. Alvim-Ferraz, M. F. Almeida, J. Rivera-Utrilla and M. Sanchez-Polo, *J Environ Manage*, 2007, **85**, 833-846.
103. E. Raymundo-Piñero, K. Kierzek, J. Machnikowski and F. Béguin, *Carbon*, 2006, **44**, 2498-2507.
104. J. Huang, B. G. Sumpter and V. Meunier, *Chemistry*, 2008, **14**, 6614-6626.
105. L.-Z. Fan, S. Qiao, W. Song, M. Wu, X. He and X. Qu, *Electrochimica Acta*, 2013, **105**, 299-304.
106. L. Zhao, L. Z. Fan, M. Q. Zhou, H. Guan, S. Qiao, M. Antonietti and M. M. Titirici, *Adv Mater*, 2010, **22**, 5202-5206.
107. B. E. Conway, Birss, V., Wojtowicz, J., , *Journal of Power Sources* 1997 **66**, 1-14.
108. D. Hulicova, Yamashita, J., Soneda, Y., Hatori, H., Kodama, M., , *Chem. Mater.*, 2005 **17** 1241-1247
109. Z. Geng, Q. Xiao, H. Lv, B. Li, H. Wu, Y. Lu and C. Zhang, *Sci Rep*, 2016, **6**, 30049.
110. K. Xie, Y. Hu, S. Afonaa-Mensah, C. Yuan, B. Cao, S. Wang and Q. Wang, *Journal of Renewable Materials*, 2022, **10**, 541-560.
111. D. W. Wang, F. Li, L. C. Yin, X. Lu, Z. G. Chen, I. R. Gentle, G. Q. Lu and H. M. Cheng, *Chemistry*, 2012, **18**, 5345-5351.



112. M. Borghei, N. Laocharoen, E. Kibena-Pöldsepp, L.-S. Johansson, J. Campbell, E. Kauppinen, K. Tammeveski and O. J. Rojas, *Applied Catalysis B: Environmental*, 2017, **204**, 394-402.
113. A. Ilnicka and J. P. Lukaszewicz, *Materials Science and Engineering: B*, 2015, **201**, 66-71.
114. R. G. Pereira, C. M. Veloso, N. M. da Silva, L. F. de Sousa, R. C. F. Bonomo, A. O. de Souza, M. O. d. G. Souza and R. d. C. I. Fontan, *Fuel Processing Technology*, 2014, **126**, 476-486.
115. A. C. Lua and T. Yang, *J Colloid Interface Sci*, 2005, **290**, 505-513.
116. M. A. El-Nemr, M. A. Hassaan and I. Ashour, *Biomass Conversion and Biorefinery*, 2022, DOI: 10.1007/s13399-022-03655-y.
117. K. Sun, J. Li, H. Peng, E. Feng, G. Ma and Z. Lei, *Ionics*, 2016, **23**, 985-996.
118. Y. Li and B. Qi, *Electrochemistry Communications*, 2023, **152**.
119. P. Williams and A. Reed, *Biomass and Bioenergy*, 2006, **30**, 144-152.
120. K. Zou, Z. Guan, Y. Deng and G. Chen, *Carbon*, 2020, **161**, 25-35.
121. S. Balou, S. E. Babak and A. Priye, *ACS Appl Mater Interfaces*, 2020, **12**, 42711-42722.
122. T. Varila, Bergna, D., Lahti, R., Romar, H., Hu, T., Lassi, U., , *BioResources* 2017 **12** 8078-8092
123. Z. G. Liu, Huang, Y.X., Zhao, G.J., , *Bioresources* 2016 **11**, 3178-3190
124. S. Wu, P. Yan, W. Yang, J. Zhou, H. Wang, L. Che and P. Zhu, *Chemosphere*, 2021, **264**, 128557.
125. X. Liu, Y. Zhou, W. Zhou, L. Li, S. Huang and S. Chen, *Nanoscale*, 2015, **7**, 6136-6142.
126. J. Xu, B. Xue, C. Liu, C. Xia, M. Li and R. Xiao, *Sustainable Energy & Fuels*, 2021, **5**, 3884-3894.
127. W. Liu, J. Yang, S. Liu, W. Yi, Y. Sun and G. Yang, *Journal of Energy Storage*, 2022, **46**.
128. M.-y. Zhang, X.-j. Jin and Q. Zhao, *New Carbon Materials*, 2014, **29**, 89-95.
129. M.-y. Zhang, X.-j. Jin and Q. Zhao, *Carbon*, 2014, **76**.
130. L. Yue, Q. Xia, L. Wang, L. Wang, H. DaCosta, J. Yang and X. Hu, *J Colloid Interface Sci*, 2018, **511**, 259-267.
131. M. Galhetas, A. S. Mestre, M. L. Pinto, I. Gulyurtlu, H. Lopes and A. P. Carvalho, *J Colloid Interface Sci*, 2014, **433**, 94-103.
132. I. I. Gurten, M. Ozmak, E. Yagmur and Z. Aktas, *Biomass and Bioenergy*, 2012, **37**, 73-81.
133. J. Mi, X.-R. Wang, R.-J. Fan, W.-H. Qu and W.-C. Li, *Energy & Fuels*, 2012, **26**, 5321-5329.
134. T. Tay, S. Ucar and S. Karagoz, *J Hazard Mater*, 2009, **165**, 481-485.
135. W. Ruan, Y. Wang, C. Liu, D. Xu, P. Hu, Y. Ye, D. Wang, Y. Liu, Z. Zheng and D. Wang, *Journal of Analytical and Applied Pyrolysis*, 2022, **168**.
136. Z. Ma, Y. Zhang, C. Li, Y. Yang, W. Zhang, C. Zhao and S. Wang, *Bioresour Technol*, 2019, **292**, 122034.
137. F. Sun, J. Gao, Y. Yang, Y. Zhu, L. Wang, X. Pi, X. Liu, Z. Qu, S. Wu and Y. Qin, *Carbon*, 2016, **109**, 747-754.
138. W. Yu, F. Lian, G. Cui and Z. Liu, *Chemosphere*, 2018, **193**, 8-16.
139. Y. Ding, Y. Li, Y. Dai, X. Han, B. Xing, L. Zhu, K. Qiu and S. Wang, *Energy*, 2021, **216**.
140. C. H. Hsu, Z. B. Pan, H. T. Qu, C. R. Chen, H. P. Lin, I. W. Sun, C. Y. Huang and C. H. Li, *RSC Adv*, 2021, **11**, 15738-15747.
141. X. Liu, X., Zuo, S.L., Cui, N.N., Wang, S.S., , 2022.
142. S. Pérez-Rodríguez, D. Sebastián, C. Alegre, T. Tsoncheva, N. Petrov, D. Paneva and M. J. Lázaro, *Electrochimica Acta*, 2021, **387**.
143. L. Xiaorui, Y. Haiping, T. Yuanjun, Y. Chao, J. Hui and X. Peixuan, *Bioresource Technology*, 2024, **403**, 130865.
144. H. Liao, S. Fan, W. Han, M. Wang, Q. Shi, Y. Xie, X. Yang and W. Chen, *Journal of Energy Storage*, 2024, **100**, 113548.
145. L. Cheng, Y. Ji and X. Liu, *Chemical Engineering Science*, 2021, **233**.
146. L. Cheng, Y. Ji, X. Liu, L. Mu and J. Zhu, *Chemical Engineering Science*, 2021, **242**.
147. Y. Cheng, S. Zhao, H. Li, S. He, J.-P. Veder, B. Johannessen, J. Xiao, S. Lu, J. Pan, M. F. Chisholm, S.-Z. Yang, C. Liu, J. G. Chen and S. P. Jiang, *Applied Catalysis B: Environmental*, 2019, **243**, 294-303.
148. X. Zhang, H. N. Tran, Y. Liu, C. Yang, T. Zhang, J. Guo, W. Zhu, M. Ahmad, H. Xiao and J. Song, *Journal of Cleaner Production*, 2023, **383**.
149. L. Ye, Y. Ying, D. Sun, Z. Zhang, L. Fei, Z. Wen, J. Qiao and H. Huang, *Angew Chem Int Ed Engl*, 2020, **59**, 3244-3251.
150. X. Wang, X. Li, S. Ding, Y. Chen, Y. Liu, M. Fang, G. Xiao and Y. Zhu, *Nano Energy*, 2021, **90**.
151. T. L. Dinadayalane, J.; Alzaaqui, N. F.; Herath, D.; Hill, B.; Campbell, A. E. , in *Elsevier*, Elsevier, Amsterdam Netherlands 2022, vol. 21, ch. 6, pp. 211-248.
152. C. Zhan, Y. Zhang, P. T. Cummings and D. E. Jiang, *Phys Chem Chem Phys*, 2016, **18**, 4668-4674.
153. M. Yang and Z. Zhou, *Adv Sci (Weinh)*, 2017, **4**, 1600408.
154. D. Adekoya, X. Gu, M. Rudge, W. Wen, C. Lai, M. Hankel and S. Zhang, *Advanced Functional Materials*, 2018, **28**.
155. Y. Xu, C. Wang, P. Niu, Z. Li, L. Wei, G. Yao, F. Zheng and Q. Chen, *Journal of Materials Chemistry A*, 2021, **9**, 16150-16159.
156. Y. Xu, C. Zhang, M. Zhou, Q. Fu, C. Zhao, M. Wu and Y. Lei, *Nature communications*, 2018, **9**, 1720.
157. X. Chang, X. Zhou, X. Ou, C. S. Lee, J. Zhou and Y. Tang, *Advanced Energy Materials*, 2019, **9**, 1902672.
158. H. Li, M. Tang, X. Huang, L. Wang, Q. Liu and S. Lu, *Chemical Engineering Journal*, 2023, **466**, 143095.



No primary research results, software or code have been included and no new data were generated or analysed as part of this review.

[View Article Online](#)

[DOI: 10.1039/D5SU00555H](#)

